KU LEUVEN

FACULTY OF SCIENCE

Ab Initio Molecular Dynamics Simulations of Phosphate Hydrolysis Using Neural Network Potentials

Albert MAKHMUDOV

Supervisor: Prof. J. Harvey
KU Leuven

Thesis presented in
fulfillment of the requirements
for the degree of Master of Science
in Theoretical Chemistry and Computational Modelling

Academic year 2024-2025

Foreword

Contribution statement

Albert Makhmudov proposed revisiting phosphate hydrolysis using a more advanced computational setup. Prof. Jeremy Harvey suggested the investigation of a system containing methyl diphosphate and proposed the use of a neural network potential to describe the reaction mechanism. The overall workflow was designed together by Albert Makhmudov and Prof. Jeremy Harvey, who also jointly analysed the results. All calculations, figures, and visualisations were carried out by Albert Makhmudov. The thesis was written by Albert Makhmudov with feedback and corrections from Prof. Jeremy Harvey.

Summary

List of abbreviations

ADP adenosine diphosphate

AIMD *ab initio* molecular dynamics

ATP adenosine triphosphate

BOMD Born-Oppenheimer molecular dynamics

CN coordination number

CSVR canonical sampling through velocity-rescaling

CV collective variable

DFT density functional theory

DFTB density functional tight-binding

DNA deoxyribonucleic acid

FES free energy surface

GGA generalised gradient approximation

GNN graph neural network

GPW Gaussian plane wave method

GTH Goedecker-Teter-Hutter pseudopotentials

lg leaving group

MD molecular dynamics

MAE mean absolute error

MeDP methyl diphosphate trianion

MeHDP methyl diphosphate dianion

MeHMP methyl phosphate monoanion

MeMP methyl phosphate dianion

MeTP methyl triphosphate tetranion

MFEP minimum free energy path

MSE mean squared error

NNP neural network potential

NPT constant number of particles, pressure and temperature

Nuc nucleophile

NVT constant number of particles, volume and temperature

PBC periodic boundary conditions

PBE Perdew-Burke-Ernzerhof exchange-correlation functional

P_i inorganic phosphate

PME Particle Mesh Ewald

polyP polyphosphate

PT proton transfer

RDF radial distribution function

RMSE root mean square error

RNA ribonucleic acid

RRHO Rigid-Rotor Harmonic-Oscillator

SCF self-consistent field

TS transition state

TZV2P triple-ζ valence basis set with two polarisation functions

WTMetaD well-tempered metadynamics

xTB extended tight-binding

Contents

Chapter 1

Introduction

This chapter provides an overview of the role of phosphates in biological systems, the enzymes involved in phosphate hydrolysis, and a detailed explanation of the reaction mechanisms associated with these processes–topics that have puzzled researchers for a long time. The discussion begins with the fundamental importance of phosphates in life, particularly in energy transfer and storage. This is followed by a brief overview of the enzymes that catalyse phosphate hydrolysis and their implications for cellular function. Finally, the chapter explores the reaction mechanisms of phosphate hydrolysis, highlighting key studies and findings in this area.

1.1 Role of phosphates in biological systems

Phosphates are among the fundamental building blocks that play a central role in life on Earth. They form the basis for both the storage and transfer of genetic information, as well as the flow of metabolic energy within biological systems. The ubiquitous nature of phosphate esters and anhydrides - such as those found in deoxyribonucleic acid (DNA), ribonucleic acid (RNA), adenosine triphosphate (ATP), and polyphosphate (polyP) - highlights their fundamental importance [1]. Some of the phosphates found in biological systems and their respective functions are summarised in Table 1.1.

A key characteristic enabling these roles is the ability of phosphoric acid to link molecular units while retaining an ionisable group. This inherent negative charge at physiological pH serves a dual purpose: it helps to retain these molecules within cellular boundaries defined by lipid membranes, and more importantly, it confers kinetic stability upon phosphate esters and anhydrides by electrostatically repelling nucleophilic attack, particularly from water [1]. For instance, the half-time for hydrolysis at 25 ℃ for a phosphomonoester monoanion (P-O) is about 90 years; however, for a phosphodiester anion (P-O), this number increases dramatically to approximately 16 million years

[2]. This stability is crucial for maintaining the integrity of genetic material but can be readily overcome by enzymatic catalysis when there is a metabolic demand.

Phosphates are involved in numerous processes in living systems, such as cell signalling and sensation, regulation of metabolism, blood coagulation, and bone formation [3, 4]. Their role is perhaps most evident in cellular energetics, where ATP functions as the universal energy currency. The energy derived from nutrients such as glucose is captured and stored within the high-energy phosphoanhydride bonds linking the phosphate groups of ATP. This energy is released upon hydrolysis of the terminal phosphoanhydride bond (P-O bond between β and γ in Figure 1.1), typically yielding adenosine diphosphate (ADP) and inorganic phosphate (P_i). The cleavage of this bond provides the thermodynamic driving force for the majority of cellular processes, including biosynthesis, active transport, and mechanical work such as muscle contraction. The standard free energy change for ATP hydrolysis is substantial ($\Delta G^0 = -30.5$ kJ mol^{-1}), and under cellular conditions, the actual free energy release is often considerably greater. Specifically, the experimentally obtained ΔG values are approximately -59 to -53.5 kJ mol^{-1} in the liver and about -61.7 to -59.5 kJ mol^{-1} in the heart [3].

Beyond ATP, polyP - a linear polymer of orthophosphate residues linked by similar high-energy phosphoanhydride bonds - represents another significant phosphate-based energy storage found across all domains of life, including mammalian cells. However, in mammalian cells, the concentration of polyP is significantly lower compared to that in microorganisms. While its roles in mammals are still being fully eluci-

Phosphate	Biological role
DNA/RNA	Genetic material
ADP/ATP	Intracellular energy transfer
cAMP	Cellular signalling
Polyphosphate	Energy storage, Cellular signalling
Creatine phosphate	Intracellular energy transfer
Phosphoenolpyruvate	Metabolism
Pyridoxal phosphate	Coenzyme
Nicotine adenine dinucleotide	Calcium signalling
Fructose 1,6-diphosphate	Metabolism
Glucose-6-phosphate	Metabolism
Isopentenyl pyrophosphate	Metabolism
Ribose-6-phosphate	Metabolism
Glycerol 3-phosphate	Metabolism
Dihydroxyacetone phosphate	Calvin cycle, metabolism
Inositol phosphates	Cellular signalling

Table 1.1: Examples of biologically relevant phosphates and their roles. Reproduced and adapted from [5].

dated, polyP metabolism is intrinsically linked to the cellular energy status. Mitochondrial polyP levels fluctuate with respiratory activity and appear to depend on F_0F_1-ATP synthase function, suggesting a role in mitochondrial bioenergetics, potentially acting as an energy reservoir [6].

The efficient transfer of energy stored in phosphate bonds from sites of production (e.g., mitochondria) to sites of utilisation (e.g., ATPases involved in muscle contraction or ion transport) is crucial. Simple diffusion of ATP is often insufficient due to the complexity of intracellular architecture and the potential for large concentration gradients to arise, which would be thermodynamically inefficient. Instead, cells employ phosphotransfer networks, utilising enzymes such as creatine kinase and adenylate kinase, which catalyse phosphoryl exchange reactions. These networks act as 'phosphoryl wires', facilitating the efficient conduction of high-energy phosphoryl groups and energetic signals throughout the cell with minimal energy dissipation or accumulation of inhibitory products such as ADP. The existence of these networks underscores the dynamic and highly organised nature of cellular energy management, where phosphates - mainly in the form of ATP - serve as the key energy carriers [7].

The synthesis of ATP occurs primarily through oxidative phosphorylation in mitochondria, a process tightly coupled to the electron transport chain, which establishes a proton-motive force (Δp) across the inner mitochondrial membrane. This electrochemical potential energy is used by the molecular machine ATP synthase. Interestingly, the principal energy input required by ATP synthase is not for the chemical formation of the phosphoanhydride bond itself, but rather for the conformational changes necessary to release the newly synthesised, tightly bound ATP molecule from the enzyme's catalytic site. This 'binding change mechanism' involves the cooperative, sequential action of the enzyme's multiple catalytic sites, driven by proton flow. The hydrolysis of ATP to ADP and P_i is catalysed by a variety of enzymes, including ATPases and possibly F_1-ATPase, which are frequently coupled to other cellular processes [8].

In summary, the unique chemical properties of phosphates - their ability to form stable esters and energy-rich anhydrides, along with their negative charge - combined with the evolution of sophisticated enzymatic machinery for their synthesis, transfer, and hydrolysis, have secured their vital role in virtually all life processes.

1.2 Enzymes involved in phosphate hydrolysis

The hydrolysis of high-energy phosphoanhydride bonds, particularly the terminal bond in ATP, is a cornerstone of cellular bioenergetics. While numerous enzymes utilise ATP hydrolysis, the F_0F_1-ATP synthase complex, primarily known for synthesising ATP,

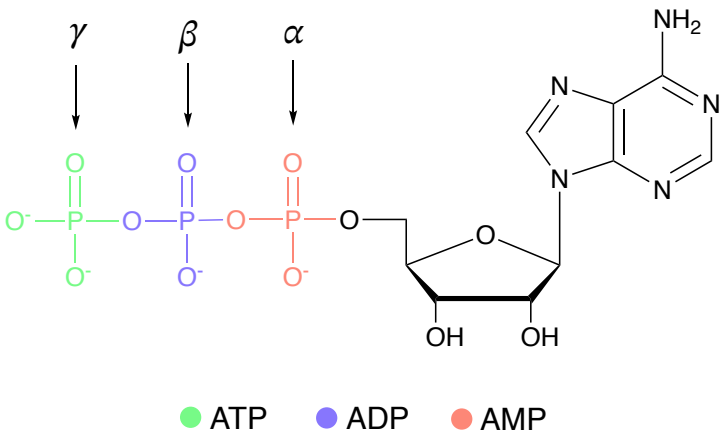

Figure 1.1: Chemical structures of the AMP, ADP, and ATP molecules with the phosphates marked as α, β, and γ, respectively.

also shows potential ATP hydrolytic activity, particularly through its F_1 component (F_1-ATPase). This enzyme complex, therefore, plays a dual role in managing the cell's primary energy currency [8–10]. Furthermore, recent evidence suggests that this complex may also participate in the metabolism, including the hydrolysis, of polyP in mammalian cells [11, 12].

The F_0F_1-ATP synthase is a molecular motor embedded in the mitochondrial membrane. It consists of two major domains: the F_1 domain, which carries the catalytic sites, and the F_0 domain, which is embedded within the membrane. These domains are connected by a central rotor stalk and a peripheral stator stalk [10, 13, 14]. The activity of this enzyme is coupled with the electron-transport chain, as illustrated in Figure 1.2.

The F_1 domain ($\alpha_3\beta_3\gamma\delta\epsilon$ stoichiometry) extends into the mitochondrial matrix. It has a globular shape as can be seen in Figure 1.2. The catalytic sites for ATP synthesis and hydrolysis are located on the three β subunits, which interact with the α subunits. When functioning in reverse, the F_1 domain acts as an F_1-ATPase, hydrolysing ATP. This hydrolysis drives the counterclockwise rotation (as viewed from the membrane) of the central stalk, composed of the γ, δ, and ϵ subunits [8, 10, 13]. If coupled to the F_0 domain, this rotation actively pumps protons from the matrix, thereby generating or maintaining the proton-motive force (Δp). This reverse function is especially important under conditions of low Δp, where it helps prevent its complete dissipation at the expense of cellular ATP and possibly polyP [9, 10, 12].

The mechanism of ATP hydrolysis (cleavage of the P-O bond between β and γ in Figure 1.1) follows the principles of the binding change mechanism [10]. The rotation of the asymmetric γ subunit induces sequential conformational changes in the three β subunits, cycling them through states analogous to those in synthesis: an 'open' state that binds ATP, a 'tight' state that facilitates hydrolysis, and a subsequent 'open' state

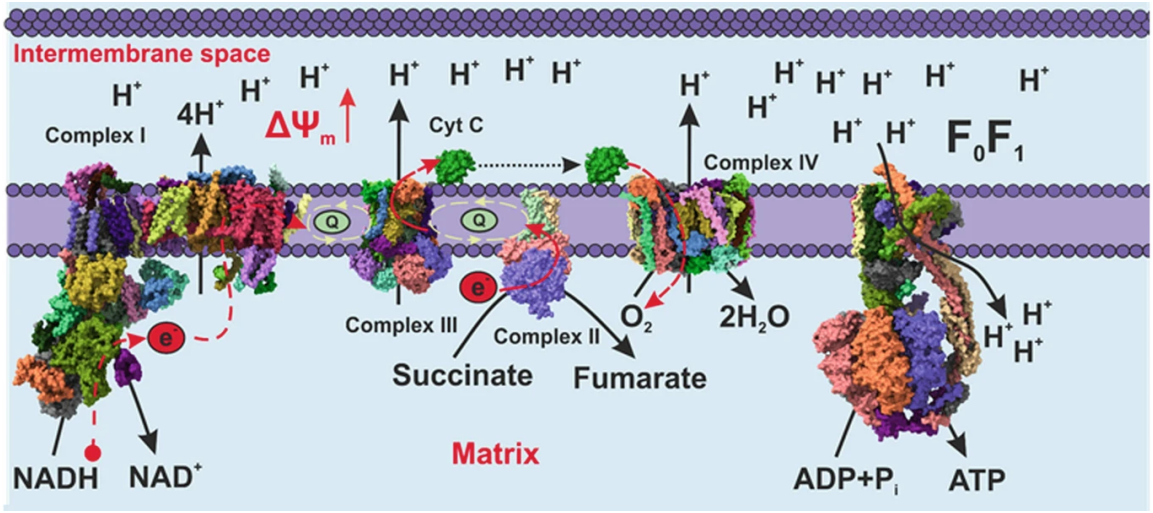

Figure 1.2: Electron transport chain coupled with oxidative phosphorylation in mitochondria. This figure was taken from [11].

that releases ADP and P_i [8, 13]. The hydrolysis of each ATP molecule is associated with a 120° rotation of the central stalk, which occurs in substeps [10].

While the metabolism of inorganic polyP is well-characterised in microorganisms via specific kinases (PPK) and phosphatases (PPX), the enzymes responsible for its turnover in mammalian cells remain largely unknown. Recent studies using immunocaptured F_0F_1-ATPase have demonstrated that the enzyme complex can hydrolyse polyP. This polyP hydrolysis appears to drive the enzyme's proton-pumping activity, akin to ATP hydrolysis, and is sensitive to oligomycin, a specific F_0F_1-ATP synthase inhibitor. Medium- and long-chain polyP molecules, made of 60 and 130 orthophosphate units, respectively, seem to be effective substrates for this hydrolytic activity. Docking simulations support the feasibility of polyP binding to the nucleotide-binding sites within the F_1 domain. This suggests that polyP could serve as an alternative energy source for the F_0F_1 complex, potentially helping to maintain mitochondrial membrane potential when ATP levels are compromised [11, 12].

There is growing confidence that the F_1-ATPase could act not only as an ATP hydrolase but also potentially as a polyP hydrolase. However, other enzymes contribute to phosphate metabolism as well. In the context of polyP, mammalian enzymes such as alkaline phosphatase (ALP) have demonstrated exopolyphosphatase activity, capable of degrading polyP chains of various lengths [11].

The world of enzymes - and phosphate hydrolysis by F_1-ATPase in particular - is both fascinating and complex. The F_1-ATPase is a molecular machine capable of hydrolysing ATP and polyP, yet the precise mechanism of hydrolysis remains not well understood. In order to address this gap, it is necessary to investigate the fundamental reaction mechanisms of phosphate hydrolysis, beginning with the simplest phosphate

esters in less complex environments such as bulk water.

1.3 Reaction mechanism: phosphate monoesters

Computational and experimental studies have provided significant insights into the mechanisms of phosphate hydrolysis reactions. Various systems and methodologies have been employed to explore the details of these fundamental biological processes. The debate often centres on whether the reaction proceeds via an associative mechanism (bond formation precedes bond breaking) or a dissociative mechanism (bond breaking precedes bond formation), and the nature of the proton transfer.

1.3.1 Phosphates

Starting from the simplest possible system, it has been shown that the hydrolysis of methyl phosphate dianion (MeMP) in water can proceed via either associative or concerted mechanisms [5, 15–17]. A schematic representation of these mechanisms is presented in Figure 1.3, which illustrates the More O'Ferrall-Jencks (MFJ) diagram. The MFJ plot is a useful two-dimensional graphical representation of multidimensional free energy surfaces.

The associative mechanism may proceed in two ways: stepwise (A_N + D_N, where A_N stands for nucleophilic addition and D_N for nucleophilic departure) or concerted (A_ND_N). The stepwise mechanism involves two transition states and an intermediate. In contrast, the concerted mechanism proceeds through a single transition state without the formation of intermediates [17].

In the case of the associative/stepwise mechanism (A_N + D_N, Figure 1.4), the nucleophile (Nuc) approaches the phosphorus atom while the leaving group (lg) is still attached. Upon the nucleophile's approach, a concerted proton transfer (PT) occurs to one of the non-bridging oxygens. The reaction proceeds through a compact pentacoordinated transition state with a trigonal bipyramidal geometry, followed by a compact intermediate and the elimination of the leaving group in a subsequent transition state.

Regarding the associative/concerted mechanism (A_ND_N), it proceeds in a manner quite similar to the first step of the associative/stepwise pathway. The reaction also involves a compact transition state in which bond formation and bond cleavage occur simultaneously.

It has been shown that the protonation state of methyl phosphate lowers the overall barrier height of the rate-limiting step; however, it does not alter the reaction mechanism [18]. For the methyl phosphate monoanion (MeHMP), the calculated barrier

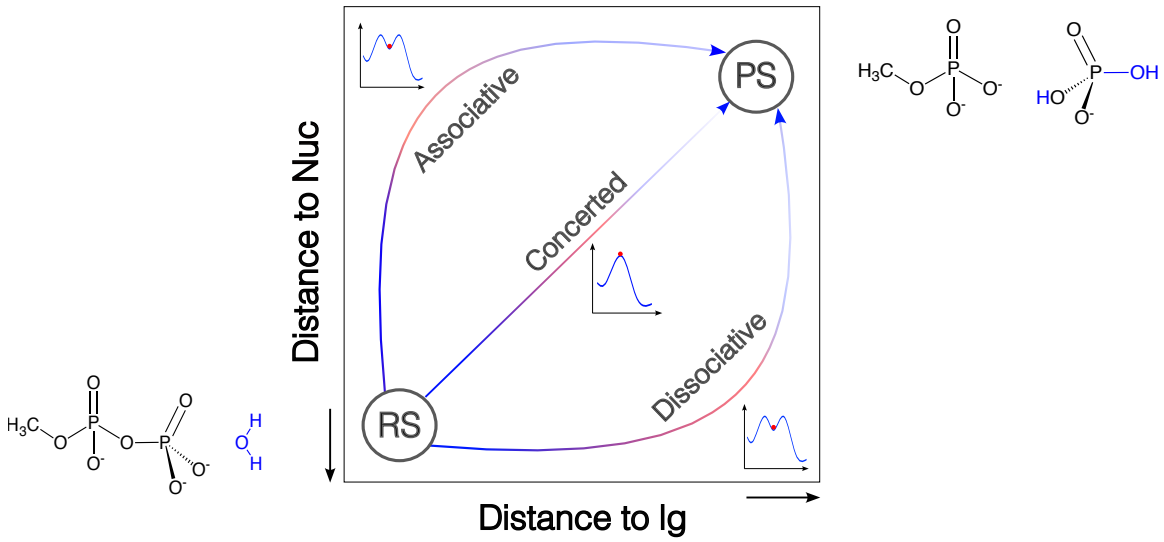

Figure 1.3: More O'Ferrall-Jencks (MFJ) plot of the possible reaction mechanisms for phosphate hydrolysis. The plot shows the free energy as a function of two reaction coordinates: the distance between phosphorus and the nucleophile (Nuc), and the distance between the leaving group (lg) and the phosphorus atom. RS stands for reactant state, PS for product state.

height $\Delta G^{\ddagger}_{calc}$ is approximately 6-7 kcal/mol lower than that of the MeMP. A similar effect was observed when OH^- acted as a nucleophile instead of a water molecule [16] (40 vs 47 kcal/mol, respectively). The latter fact arises a question about the proton-transfer in this reaction, for instance, whether it could happen in a concerted or a stepwise manner, in which the PT happens in the pre-equillibration phase.

For the associative mechanism, calculated barrier heights $\Delta G^{\ddagger}_{calc}$ lie in the range of 33.7-47.2 kcal/mol, while experimental values obtained at 25 ℃ range between 30.6 and 44.3 kcal/mol, depending on the protonation state. Detailed information about the calculated and experimentally determined barrier heights can be found in Table 1.2. Corresponding data on transition state structures and intermediates is summarised in Table 1.3.

The concerted mechanism (A_ND_N) is characterised by a single transition state where the nucleophile approaches the phosphorus atom while the leaving group remains attached. The reaction proceeds via a compact pentacoordinated transition state with a trigonal bipyramidal geometry, which is more expansive compared to that of the associative mechanism (Table 1.3). In this transition state, the distance between the phosphorus atom and the nucleophile is approximately 2.06-2.75 Å, while the distance between the leaving group and the phosphorus atom is around 2.61-2.75 Å. The barrier heights for the concerted mechanism are 44.5 and 47 kcal/mol (Table 1.2).

As can be observed, it is rather difficult to clearly distinguish between the associative and concerted mechanisms, and it appears that both may occur in bulk water. Even by looking at the activation entropies of both reaction pathways, it's clear that the

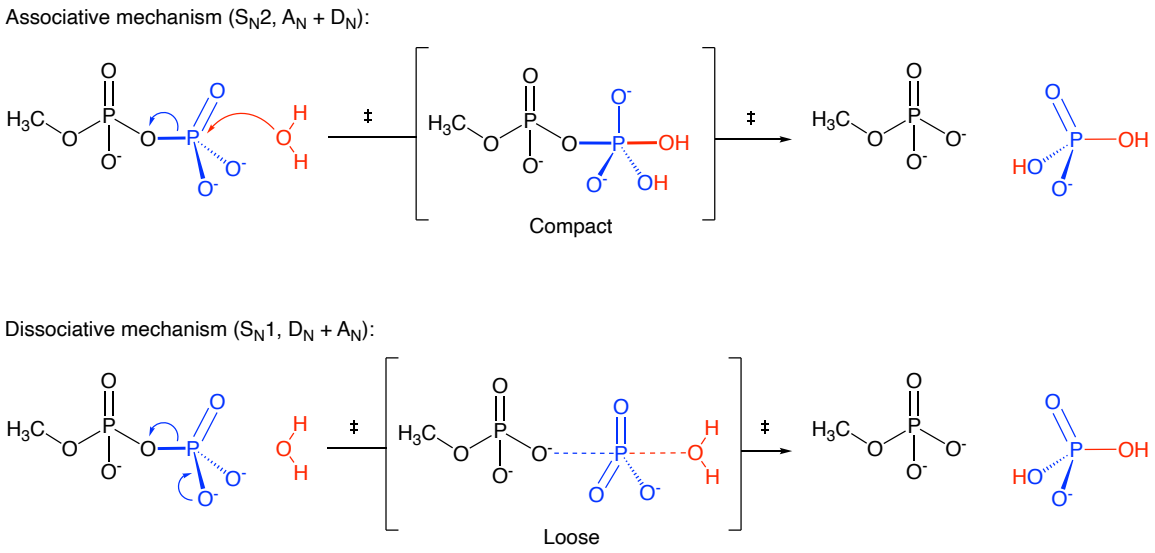

Figure 1.4: Associative and dissociative reaction mechanisms. For the transition states, only one of the two is shown. The nucleophile (Nuc) is shown in red, the leaving group (lg) in black, and the phosphoryl group in blue.

corresponding values are similarly small: 0.7 and -1.6 kcal/mol for the associative and concerted mechanisms, respectively [17]. Nevertheless, the dissociative mechanism is unlikely to take place, or at least it has not been observed.

1.3.2 Diphosphates

Moving on to more complex systems, the hydrolysis of pyrophosphates (diphosphates), namely methyl diphosphate trianion (MeDP), has also been thoroughly studied. It has been shown that the reaction mechanism can proceed through either associative or concerted pathways, just as in the case of methyl phosphate. In contrast, the associative mechanism has been demonstrated to be solely concerted. However, there is a twist to this story: the dissociative mechanism has also been observed, in both concerted and stepwise forms [15, 16, 19]. A schematic representation of the mechanisms can be found in Figures 1.3 and 1.4.

In the associative/concerted mechanism, the reaction undergoes the same steps as discussed in Subsection 1.3.1. The transition state has a similarly compact geometry: the distance between the phosphorus atom and the nucleophile is approximately 2.03–2.26 Å, and the distance between the leaving group and the phosphorus atom is around 1.82–2.4 Å, as shown in Table 1.3. However, the calculated barrier heights are slightly lower in comparison to methyl phosphate, ranging from 34 to 38 kcal/mol (Table 1.2).

The concerted pathway is characterised by the same general mechanism as discussed in Subsection 1.3.1. The transition state is more expansive than in the associative mechanism, with the distance between the phosphorus atom and the nucleophile

Table 1.2: Summary of computational and experimental studies on phosphate hydrolysis. In the case of calculated $\Delta G^{\ddagger}$, the rate-limiting step is given. [1]The values were calculated using the transition state theory (TST).

System	Method	Level of theory	Mechanism	$\Delta G^{\ddagger}$ (kcal/mol)	Ref.
$MeMP^{2-}$ + H_2O	DFT	B3LYP/6-311+G** and COSMO	Associative Concerted	47.2 44.5	[15]
$MeMP^{2-}$ + H_2O	DFT	B3LYP/6-311++G** and COSMO	Associative	47	[16]
$MeMP^{2-}$ + 3 H_2O	DFT	M06-2X/6-311+G** and SMD	Associative Concerted	$\approx$ 36 $\approx$ 44	[17]
$MeMP^{2-}$ + 4 H_2O	DFT	M06-2X/6-311+G**	Associative	$\approx$ 40.8$\pm$1.9	[18]
$MeHMP^{-}$ + 4 H_2O	DFT	M06-2X/6-311+G**	Associative	$\approx$ 33.7$\pm$1.7	[18]
$MeDP^{3-}$ + 2 H_2O	DFT	B3LYP/6-311++G** and PCM	Associative Dissociative	34.64 35.24	[19]
$MeDP^{3-}$ + H_2O	DFT	B3LYP/6-311+G** and COSMO	Associative Dissociative	34.8 30.3	[15]
$MeDP^{3-}$ + H_2O	DFT	B3LYP/6-311++G** and COSMO	Associative Concerted	38 34	[16]
$MeHDP^{2-}$ + H_2O	DFT	B3LYP/6-311++G** and COSMO	Associative Concerted	34 31	[16]
$MeDP^{3-}$ + Mg^{2+} + 5 H_2O	QM/MM, FEP (EVB)	B3LYP/6-311++G** and MM	Associative Concerted Dissociative	35 34 35	[16]
$MeTP^{4-}$ + Mg^{2+} + 54 H_2O	CPMD	PBE/PW with Troullier-Martins pseudopotentials	Associative Concerted Dissociative	39.1 35.1 36.6	[20]
$MeTP^{4-}$ + Mg^{2+} + 113 H_2O	BOMD, metadynamics	BLYP/TZV2P with GTH pseudopotentials	Associative Concerted	29 29-30	[21]
ATP^{4-} + Mg^{2+} + 4163 H_2O + counterions	QM/MM, NEB	B3LYP/6-311++G** and MM	Concerted	32.5	[22]
ATP^{4-} + Mg^{2+} + 1800 H_2O + counterions	QM/MM, QM = CPMD	BLYP/PW with Troullier-Martins pseudopotentials and MM	Associative Dissociative	36.2 33.4	[23]
Methyl phosphate dianion	Exp. at 25°C	–	–	44.3	[2]
Methyl phosphate monoanion	Exp. at 25°C	–	–	30.6	[2]
Pyrophosphate trianion	Exp. at 25°C	–	–	29.2	[2]
Pyrophosphate dianion	Exp. at 25°C	–	–	27.7	[2]
ADP^{2-} (or ATP^{3-})	Exp. at 25°C	–	–	27.5	[2]
$ATPH^{3-}$ (or ATP^{4-})	Exp. at 70°C	pH=6.69-7.66	–	24.34-24.78[1]	[24]
$dADPH^{2-}$ (or $dADP^{3-}$)	Exp. at 70°C	pH=6.82	–	24.25[1]	[25]
$dATPH^{3-}$ (or $dATP^{4-}$)	Exp. at 70°C	pH=7.00	–	24.50[1]	[25]
$MgATPH^{-}$ (or $MgATP^{2-}$)	Exp. at 70°C	pH=6.59-7.63	–	24.59-24.64[1]	[24]
$CaATPH^{-}$ (or $CaATP^{2-}$)	Exp. at 70°C	pH=6.67-7.01	–	25.71-25.72[1]	[24]

being approximately 2.26–2.5 Å, while the distance between the leaving group and the phosphorus atom is around 2.7 Å (Table 1.3). The barrier heights for the concerted mechanism are 31 and 34 kcal/mol (Table 1.2), which is notably lower than in the case of methyl phosphate.

In general, it can be noted that the barrier height is strongly dependent on the pK_a value of the leaving group. The lower the pK_a, the lower the $\Delta G^{\ddagger}$ ($pK_a(CH_3O^-)$ = 15.5 vs $pK_a(CH_3PO_4^{2-})$ = 6.3). Not only does a lower pK_a reduce the barrier height, but it also favours the concerted and dissociative mechanisms [16].

The dissociative mechanism can proceed via both concerted and stepwise routes. The dissociative/concerted pathway is quite similar to the general concerted mechanism. The main difference lies in the synchrony of the transition state: while the general concerted mechanism has a more synchronous transition state, the dissociative/concerted one features a greater distance between the phosphorus atom and the leaving group.

On the other hand, the dissociative/stepwise pathway ($D_N + A_N$) is characterised by the departure of the leaving group from the phosphorus atom before the nucleophile approaches. Thus, there is clearly no bond remaining between the phosphorus and the leaving group. Following the departure of the leaving group, a planar metaphosphate PO_3^- is formed, as illustrated in Figure 1.4. The transition state is more expansive compared to that of the associative mechanism, with the distance between the phosphorus atom and the nucleophile being 2.7 Å, and the distance between the leaving group and the phosphorus atom being 3.4 Å (Table 1.3). Consequently, after TS_1, the system reaches an intermediate step in which the nucleophile is positioned closer to the metaphosphate, followed by an attack and bond formation in TS_2.

The barrier heights for the dissociative mechanism lie in the range of 30.3–35.24 kcal/mol (Table 1.2), which is lower than those for any of the previously mentioned mechanisms. Comparing the calculated and experimentally obtained $\Delta G^{\ddagger}$ clearly indicates that the dissociative mechanism is more favourable than the associative and concerted ones. The $\Delta G^{\ddagger}_{exp}$ values for the pyrophosphate trianion and dianion are 29.2 and 27.7 kcal/mol, respectively. The influence of one-water (1W) or two-water (2W) mechanisms has also been explored [19], but the overall barriers remain similar.

The dissociative mechanism is further favoured by the presence of metal ions, such as Mg^{2+}, as well as in cases where MeDP is protonated, i.e. methyl diphosphate dianion (MeHDP). Interestingly, in the latter case, the proton always transfers to the leaving group en route to the product state [16].

Even though computational studies suggest that Mg^{2+} promotes the dissociative mechanism, experimental data do not support this hypothesis [24], since the $\Delta G^{\ddagger}_{exp}$ obtained at 70 ℃ shows little to no difference, at least in the case of adenosine triphos-

Table 1.3: Summary of the distances between the phosphorus atom and the nucleophile as well as the leaving group in the transition states and intermediates. All distances are in Å.

System	Mechanism	TS_1		Intermediate		TS_2		Ref.
		d(P-O_{Nuc})	d(P-O_{lg})	d(P-O_{Nuc})	d(P-O_{lg})	d(P-O_{Nuc})	d(P-O_{lg})	
$MeMP^{2-}$	Associative (A_ND_N)	2.0	1.8	–	–	–	–	[16]
	Associative (A_ND_N)	1.9	2.15	–	–	–	–	[15]
	Associative ($A_N + D_N$)	2.16	1.71	1.84	1.78	1.71	2.24	[17]
	Associative ($A_N + D_N$)	2.08	1.78	1.99	1.80	1.77	2.52	[18]
	Concerted (A_ND_N)	2.75	2.75	–	–	–	–	[15]
	Concerted (A_ND_N)	2.06	2.61	–	–	–	–	[17]
$MeHMP^{-}$	Associative ($A_N + D_N$)	2.26	1.66	1.76	1.77	1.68	2.25	[18]
$MeDP^{3-}$	Associative (A_ND_N)	2.2	2.0	–	–	–	–	[15]
	Associative (A_ND_N)	2.03	1.88	–	–	–	–	[16]
	Associative (A_ND_N)	2.2	2.0	–	–	–	–	[19]
	Concerted (A_ND_N)	2.5	2.7	–	–	–	–	[16]
	Dissociative (A_ND_N)	2.8	3.25	–	–	–	–	[15]
	Dissociative ($D_N + A_N$)	2.7	3.4	2.0	3.75	1.7	3.75	[19]
$MeDP^{3-}$ + Mg^{2+}	Associative (A_ND_N)	2.1	2.4	–	–	–	–	[16]
	Concerted (A_ND_N)	2.3	2.7	–	–	–	–	[16]
	Dissociative (A_ND_N)	2.8	3.4	–	–	–	–	[16]
$MeHDP^{2-}$	Associative (A_ND_N)	2.26	1.82	–	–	–	–	[16]
	Concerted (A_ND_N)	2.26	2.78	–	–	–	–	[16]
$MeTP^{4-}$ + Mg^{2+}	Associative (A_ND_N)	1.9	2.0	–	–	–	–	[20]
	Associative ($A_N + D_N$)	2.03	3.11	1.95	3.06	1.66	3.26	[21]
	Concerted (A_ND_N)	2.5	2.6	–	–	–	–	[20]
	Concerted (A_ND_N)	2.28	2.69	–	–	–	–	[21]
	Dissociative (A_ND_N)	3.6	3.5	–	–	–	–	[20]
ATP^{4-} + Mg^{2+}	Associative (A_ND_N)	1.9	1.9	–	–	–	–	[23]
	Concerted (A_ND_N)	2.8	3.2	–	–	–	–	[22]
	Dissociative (A_ND_N)	3.5	3.5	–	–	–	–	[22]

phate (Table 1.2).

1.3.3 Triphosphates

Last but not least, let us consider the hydrolysis of triphosphates. These systems more closely resemble the biological environment, particularly the processes associated with energy metabolism.

The hydrolysis of methyl triphosphate tetranion (MeTP) and ATP has been studied using a range of computational methods. It has been shown that the reaction mechanisms share many similarities with those observed in mono- and diphosphates. Specifically, the mechanism may proceed via associative/concerted and associative/stepwise routes, as well as concerted and dissociative/concerted pathways (Table 1.3).

When comparing the calculated and experimentally obtained $\Delta G^{\ddagger}$ values, it is difficult to clearly distinguish between the aforementioned mechanisms. The calculated barrier heights span a range from 29 to 39.1 kcal/mol, whereas experimental data suggest that the barrier height for ATP should be around 27.5 kcal/mol, as shown in Table 1.2. The more complex the system becomes, the more factors one must likely take into account.

In summary, computational investigations reveal a nuanced and peculiar picture of phosphate hydrolysis. The preferred mechanism (associative, concerted, or dissociative) and the proton transfer route (1W, 2W, etc.) depend significantly on specific factors such as the pKa of the leaving group, the protonation state, the presence of metal ions like Mg^{2+}, and the surrounding solvent environment.

Moreover, it is important to keep in mind that in order to properly study the underlying free energy surface, adequate sampling of the reaction space is crucial. To achieve this, various free energy techniques such as metadynamics can be employed, provided that the level of theory is sufficient to describe a system of realistic size while allowing the results to be obtained within a reasonable timeframe. This is precisely the goal of the present project.

1.4 Research goals

To begin with, I'd like to quote the following line from Paul A. M. Dirac [26], which I find particularly relevant to the topic of this thesis:

> The underlying physical laws necessary for the mathematical theory of a large part of physics and the whole of chemistry are thus completely known, and the difficulty is only that the exact application of these laws leads to

equations much too complicated to be soluble. *It therefore becomes desirable that approximate practical methods of applying quantum mechanics should be developed, which can lead to an explanation of the main features of complex atomic systems without too much computation.*

Chapter 2

Theory

This chapter provides a short and condensed introduction to the theoretical concepts of the methods used in this work. It begins with a discussion of statistical mechanics and free energy techniques, followed by an overview of density functional theory and *ab initio* molecular dynamics. Finally, the chapter concludes with a brief introduction to graph neural networks and neural network potentials. The aim is to provide a comprehensive background to the methods used, while the technical details and derivations are left to the literature sources cited throughout the text.

2.1 A brief introduction to statistical mechanics

The discussion in this section is mostly based on the "Introduction to Computational Chemistry" textbook written by Jensen [27], "Statistical Mechanics: Theory and Molecular Simulation" by Tuckermann [28], and "Understanding Molecular Simulation: From Algorithms to Applications" by Frenkel and Smit [29] unless stated otherwise.

2.1.1 Partition functions

The development of the field of statistical mechanics has been crucial for the computational chemistry community, as it enables the connection between the jigglings and wigglings of atoms and the properties of much larger systems such as liquids and solids.

Let us begin with the most fundamental concept: the partition function. The partition function is akin to a Swiss army knife in statistical mechanics, meaning it is a versatile tool that makes the connection between microscopic and macroscopic properties in thermodynamics possible. In the simplest case of a single molecule, the partition function q takes the following form:

$$q = \sum_{i=\text{levels}}^{\infty} g_i e^{-\epsilon_i/kT} \tag{2.1}$$

Here, it is expressed as a sum over all energy levels ϵ_i of a molecule (or particle), multiplied by a degeneracy factor g_i in cases where multiple levels have the same energy. The term kT represents the Boltzmann factor.

Moving on to a more complex scenario in which the partition function describes multiple molecules, we arrive at the partition function Q for non-interacting particles, such as those in an ideal gas:

$$Q = q^N \text{ (different particles)} \quad Q = \frac{q^N}{N!} \text{ (identical particles)} \tag{2.2}$$

Here, N denotes the total number of particles. However, one could argue that if we wish to describe a real system such as bulk water, we must account for interactions between molecules. Consequently, Equation 2.2 must be rewritten:

$$Q = \sum_{i}^{\infty} e^{-E_i/kT} \tag{2.3}$$

In this case, the partition function Q includes contributions from all possible energy states E_i of the system.

Although the concept of the partition function might initially appear abstract, it can be clarified by expressing it in a different form, namely, within the context of the Rigid-Rotor Harmonic-Oscillator (RRHO) approximation, where the electronic, vibrational, and rotational degrees of freedom can be separated. For a single molecule case it would look like:

$$q_{\text{tot}} = q_{\text{trans}} \times q_{\text{rot}} \times q_{\text{vib}} \times q_{\text{elec}} \tag{2.4}$$

Let us now examine each contribution in more detail. From this point onward we will consider polyatomic molecules in the formulation of the partition functions, unless stated otherwise.

The translational partition function q_{trans} can be derived from the energy expression for a particle in a one-dimensional box and is given by:

$$q_{\text{trans}} = \left(\frac{2\pi MkT}{h^2}\right)^{3/2} V \tag{2.5}$$

Here, M is the total molecular mass, and V is the volume. Turning to the rotational partition function q_{rot}, it can be derived from the Schrödinger equation for a diatomic "rigid rotor" and has the following form:

$$q_{\text{rot}} = \frac{8\pi^2 IkT}{h^2\sigma} \tag{2.6}$$

In this expression, I denotes the moment of inertia, and σ represents the symmetry factor, i.e. the order of the rotational subgroup within the molecular point group. For polyatomic molecules, writing an exact expression is more complex, but an approximate form can be used:

$$q_{\text{rot}} = \frac{\sqrt{\pi}}{\sigma}\left(\frac{8\pi^2 kT}{h^2}\right)^{3/2}\sqrt{I_1 I_2 I_3} \tag{2.7}$$

For the vibrational partition function q_{vib}, it is expressed as a product over the various vibrational modes of a molecule, each with frequency ν_i:

$$q_{\text{vib}} = \prod_i \frac{e^{-h\nu_i/2kT}}{1 - e^{-h\nu_i/kT}} \tag{2.8}$$

Lastly, the electronic partition function q_{elec} is given as a sum over all electronic states of a molecule, from the ground state to all excited states. However, since the energy difference between the ground state and higher states is usually much greater than kT at ambient temperatures, the function can typically be approximated by considering only the ground state:

$$q_{\text{elec}} = \sum_{i=0}^{\infty} g_i e^{-\epsilon_i/kT} \approx g_0 e^{-\epsilon_0/kT} \tag{2.9}$$

2.1.2 Macroscopic properties and thermodynamic functions

Once the partition function is determined, it provides a direct means of evaluating macroscopic properties. For instance, the internal energy U and the Helmholtz free energy A can be calculated from the partition function Q:

$$U = kT^2\left(\frac{\partial \ln Q}{\partial T}\right)_V \tag{2.10}$$

$$A = -kT \ln Q \tag{2.11}$$

In addition, other macroscopic properties, such as pressure P and the heat capacity at constant volume C_V, can also be expressed in terms of the partition function:

$$P = -\left(\frac{\partial A}{\partial V}\right)_T = kT\left(\frac{\partial \ln Q}{\partial V}\right)_T \tag{2.12}$$

$$C_V = \left(\frac{\partial U}{\partial T}\right)_V = 2kT\left(\frac{\partial \ln Q}{\partial T}\right)_V + kT^2\left(\frac{\partial^2 \ln Q}{\partial T^2}\right)_V \tag{2.13}$$

Turning to thermodynamic functions, namely enthalpy H, entropy S, and Gibbs free energy G, these can also be derived from the partition function Q:

$$H = U + PV = kT^2\left(\frac{\partial \ln Q}{\partial T}\right)_V + kTV\left(\frac{\partial \ln Q}{\partial V}\right)_T \tag{2.14}$$

$$S = \frac{U - A}{T} = kT\left(\frac{\partial \ln Q}{\partial T}\right)_V + k\ln Q \tag{2.15}$$

$$G = H - TS = kTV\left(\frac{\partial \ln Q}{\partial V}\right)_T - kT\ln Q \tag{2.16}$$

This connection between macroscopic observables, thermodynamic functions, and the partition function once again highlights its fundamental importance in statistical thermodynamics.

2.1.3 The canonical ensemble

Having established a method to calculate the macroscopic properties of a system we implicitly relied on averaging over a large enough number of states. Therefore one may naturally ask: how can we sample enough configurations to apply the equations described in the previous section under conditions that resemble those in experiments? One such answer is the canonical ensemble.

The canonical ensemble describes a system at constant temperature T, fixed volume V, and a fixed number of particles N (NVT). In this ensemble, the system is in contact with a heat bath, which makes it particularly relevant to most molecular simulations that are describing the experimental conditions, where the temperature is externally controlled while the internal energy of the system is allowed to fluctuate.

Since the energy fluctuates in the canonical ensemble, a logical step is to estimate the magnitude of these fluctuations:

$$\frac{\Delta E}{E} \sim \frac{\sqrt{N}}{N} \sim \frac{1}{\sqrt{N}} \tag{2.17}$$

Here, N denotes the number of particles, and thus for sufficiently large systems, the relative energy fluctuations become negligible.

The use of the canonical ensemble implicitly assumes that the system is ergodic, meaning that time averages obtained from simulation trajectories are equivalent to ensemble averages over the Boltzmann distribution. This assumption is, for instance, central to molecular dynamics simulations where the canonical ensemble can be sampled.

2.1.4 Classical forcefields and molecular dynamics

Bringing all the puzzle pieces together, we can now discuss how to simulate a molecular or atomic system of interest. One widely used approach is molecular dynamics (MD) simulations. The first step involves defining a potential energy function that describes the interactions between atoms. This function, often referred to as a forcefield, is typically parameterised based on experimental data or high-level quantum mechanical calculations.

In classical MD, the evolution of a system of N atoms is governed by Newton's equations of motion. A commonly used form of the potential energy function is:

$$\begin{aligned} U(\mathbf{r}_1, \ldots, \mathbf{r}_N) = & \sum_{\text{bonds}} \frac{1}{2} K_{\text{bond}} (r - r_0)^2 + \sum_{\text{bends}} \frac{1}{2} K_{\text{bend}} (\theta - \theta_0)^2 \\ & + \sum_{\text{tors}} \sum_{n=0}^{6} A_n \left[1 + \cos(C_n \phi + \delta_n)\right] \\ & + \sum_{i,j \in \text{nb}} \left\{ \left[4\epsilon_{ij} \left(\frac{\sigma_{ij}}{r_{ij}} \right)^{12} - \left(\frac{\sigma_{ij}}{r_{ij}} \right)^{6} \right] + \frac{q_i q_j}{r_{ij}} \right\} \end{aligned} \tag{2.18}$$

Here, the total energy is decomposed into bonded interactions (bonds, angles, and torsions) and non-bonded interactions, including Lennard-Jones and Coulombic terms. Once the potential is specified, the force on each atom i is obtained via:

$$\mathbf{F}_i = -\frac{\partial U}{\partial \mathbf{r}_i} \tag{2.19}$$

To propagate the positions and velocities of atoms in time, numerical integration schemes are employed. Among these, the velocity Verlet algorithm is widely used in perhaps all MD engines. Let us consider the Taylor expansion of the position of particle i to second order in the time step Δt:

$$\mathbf{r}_i(t + \Delta t) \approx \mathbf{r}_i(t) + \Delta t\, \mathbf{v}_i(t) + \frac{\Delta t^2}{2 m_i} \mathbf{F}_i(t) \tag{2.20}$$

Here, $\mathbf{F}_i(t)$ is the force on particle i at time t, and m_i is its mass, calculated using Equation 2.19 and $\mathbf{v}_i(t)$ is its velocity. This expression provides a prediction of the new

position based on the current velocity and force.

We can also consider a backward expansion in time from $\mathbf{r}_i(t + \Delta t)$ and $\mathbf{v}_i(t + \Delta t)$, yielding:

$$\mathbf{r}_i(t) = \mathbf{r}_i(t + \Delta t) - \Delta t\, \mathbf{v}_i(t + \Delta t) + \frac{\Delta t^2}{2m_i}\mathbf{F}_i(t + \Delta t) \tag{2.21}$$

By substituting Equation 2.20 into Equation 2.21 and solving for $\mathbf{v}_i(t + \Delta t)$, we get:

$$\mathbf{v}_i(t + \Delta t) = \mathbf{v}_i(t) + \frac{\Delta t}{2m_i}\left[\mathbf{F}_i(t) + \mathbf{F}_i(t + \Delta t)\right] \tag{2.22}$$

Equations 2.20 and 2.22 together form the velocity Verlet integrator. The algorithm proceeds as follows:

1. First, update positions using Equation 2.20.
2. Then, compute new forces $\mathbf{F}_i(t + \Delta t)$ based on the updated positions.
3. Finally, update velocities using Equation 2.22.

To correctly sample the canonical ensemble, one should consider the use of thermostats to maintain the system temperature. In this work, we focus on two widely used thermostats: the Nosé–Hoover thermostat [30, 31] and the canonical sampling through velocity-rescaling (CSVR) thermostat [32]. In the former, the equations of motion are modified to include a friction term that couples the system to a heat bath, allowing for energy exchange. The CSVR thermostat, on the other hand, uses a velocity rescaling approach to maintain the desired temperature by adjusting particle velocities at each time step.

2.1.5 Enhanced sampling techniques

Even though MD simulations are a powerful tool for studying molecular systems, their applicability can be limited due to the presence of energy barriers separating minima in the potential energy landscape. As a result, the system may remain trapped in local minima, leading to insufficient sampling of the relevant configurational space. This issue becomes particularly pronounced in the context of reactive systems, where rare events involve transitions between states separated by high free energy barriers and occur on timescales much longer than typical simulation durations.

To address this challenge, various enhanced sampling techniques have been developed. These methods aim to accelerate the exploration of phase space. In general,

they bias the system along reaction coordinates, or collective variables (CVs), by applying a biasing potential that drives the system towards regions of interest. One such approach is metadynamics [33, 34].

In metadynamics, a biasing (external) potential is added to the system's potential energy surface. This biasing potential takes the following form:

$$V(S(x),t) = w \sum_{t'=\tau_G,2\tau_G,\ldots}^{t'<t} \exp\left(-\frac{(S(x)-s(t'))^2}{2\delta s^2}\right) \tag{2.23}$$

where $s(t) = S(x(t))$ is the value of the CV at time t. The height of the Gaussian kernel is denoted by w, δs is its width, and τ_G is the deposition rate.

The approach used in metadynamics can be explained using the Panama Canal as an analogy as illustrated in Figure 2.1. The idea is to fill the basins of the free energy landscape with a Gaussian potential, which can be thought of as water gradually filling the basins, lifting the system (like a ship in a lock) out of a free energy minimum and helping it traverse to other states.

The assumption in metadynamics is that, after sufficiently long sampling, the biasing potential $V_G(S,t)$ converges to the negative of the underlying free energy surface:

$$\lim_{t\to\infty} V(s,t) \sim -F(s) \tag{2.24}$$

Despite the many benefits that metadynamics offers, it is important to note that it has limitations. For example, obtaining a converged free energy surface is not straightforward, especially when multiple CVs are involved. In principle, Gaussian kernels can be deposited indefinitely, making it difficult to assess convergence. To address this issue, the well-tempered variant of metadynamics was developed [35]. In this method, a history-dependent potential is added, which is defined as:

$$V(s,t) = \Delta T \ln\left(1 + \frac{\omega N(s,t)}{\Delta T}\right) \tag{2.25}$$

Here, $N(s,t)$ is the histogram of s obtained from a biased simulation, ΔT is the biasing temperature, and ω has the dimension of an energy rate. The rate at which this potential is modified over time is given by:

$$\dot{V}(s,t) = \frac{\omega \Delta T \delta_{s,s(t)}}{\Delta T + \omega N(s,t)} = \omega e^{-[V(s,t)/\Delta T]} \delta_{s,s(t)} \tag{2.26}$$

The height of the Gaussian kernels used is:

$$w = \omega e^{-[V(s,t)/\Delta T]} \tau_G \tag{2.27}$$

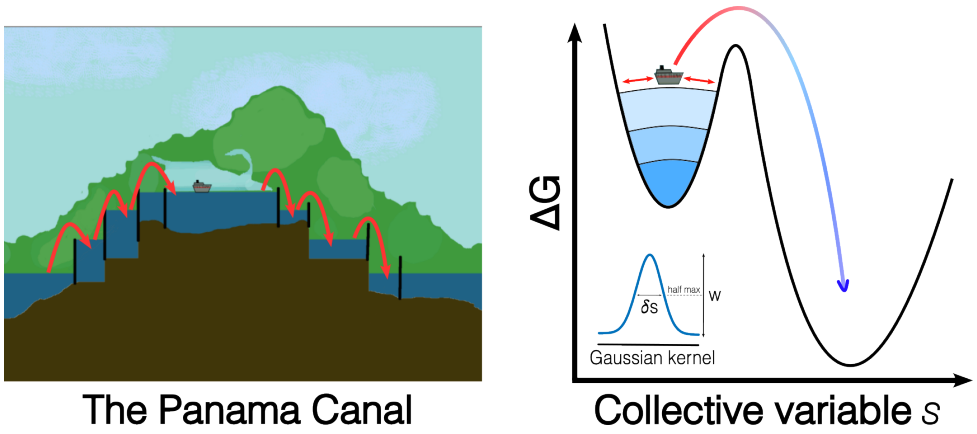

Figure 2.1: The concept of metadynamics. w stands for the Gaussian kernel height, and δs stands for its width. The Panama Canal cartoon was taken from [36].

where τ_G is the deposition rate and ω represents the initial bias deposition rate. The Gaussian kernel height is now dependent on the history of the system, allowing for a more controlled exploration of the free energy landscape.

Ultimately, the underlying free energy surface can be estimated using the following equation:

$$\tilde{F}(s,t) = -\frac{T+\Delta T}{\Delta T} V(s,t) = -(T+\Delta T)\ln\left(1+\frac{\omega N(s,t)}{\Delta T}\right) \tag{2.28}$$

The advantage of well-tempered metadynamics (WTMetaD) is that it enables more efficient exploration of the free energy landscape, as the biasing potential adapts according to the trajectory's history. Moreover, the convergence can be easily monitored by observing the decay of the Gaussian height, which should approach zero as the system fully explores the relevant phase space.

2.2 The density functional theory tourist

The discussion in this section is primarily based on the "Introduction to Computational Chemistry" textbook written by Jensen [27], "Density Functional Theory: a Practical Introduction" by Scholl and Steckel [37], and "A Chemist's Guide to Density Functional Theory" by Koch and Holthausen [38] unless stated otherwise.

2.2.1 The Kohn-Sham approach

In order to describe reactive events in relatively large systems, up to approximately 1,000 atoms, it is necessary to use methods that offer a good balance between accuracy and computational cost. One such method is density functional theory (DFT),

which is based on the Hohenberg-Kohn theorems and the Kohn-Sham equations.

The central idea behind DFT, established by Hohenberg and Kohn, is that the ground state energy of a many-electron system can be expressed as a functional of the electron density. This reformulation reduces the problem from solving a $3N$-dimensional wavefunction to working with a 3-dimensional electron density.

The energy functional can be written as:

$$\begin{aligned} E[\rho(\mathbf{r})] &= T_s[\rho] + J[\rho] + E_{Ne}[\rho] + E_{XC}[\rho] = \\ &= -\frac{1}{2}\sum_{i}^{N}\langle\phi_i|\nabla^2|\phi_i\rangle \\ &\quad + \frac{1}{2}\sum_{i}^{N}\sum_{j}^{N}\iint |\phi_i(\mathbf{r}_1)|^2 \frac{1}{r_{12}} |\phi_j(\mathbf{r}_2)|^2 \, d\mathbf{r}_1 d\mathbf{r}_2 \\ &\quad - \sum_{i}^{N}\sum_{A}^{M}\int \frac{Z_A}{r_{1A}} |\phi_i(\mathbf{r}_1)|^2 \, d\mathbf{r}_1 \\ &\quad + E_{XC}[\rho(\mathbf{r})] \end{aligned} \tag{2.29}$$

Here, the first three terms are "known" and represent the kinetic energy of the electrons, the Coulomb interaction between the electrons, and the electron-nucleus interaction, respectively. The final term, the exchange-correlation energy functional, is the unknown component. It contains all the effects that are not straightforward to treat exactly, for instance, the residual part of the kinetic energy and the non-classical electron-electron interactions:

$$E_{XC}[\rho] \equiv (T[\rho] - T_s[\rho]) + (E_{ee}[\rho] - J[\rho]) \tag{2.30}$$

The biggest challenge in DFT lies in the formulation of E_{XC}. This term is particularly important, as finding the minimum of the total energy functional, as expressed in Equation 2.29, depends on its accurate representation.

To address this, the Kohn-Sham approach introduces a set of single-electron equations that can be solved iteratively to obtain the electron density and the total energy of the system. The Kohn-Sham equations are given by:

$$\left(-\frac{1}{2}\nabla^2 + V_{eff}(\mathbf{r})\right)\phi_i = \varepsilon_i\phi_i \tag{2.31}$$

Here, V_{eff} takes the form:

$$V_{eff}(\mathbf{r}) = \int \frac{\rho(\mathbf{r}_2)}{r_{12}} d\mathbf{r}_2 + V_{XC}(\mathbf{r}) - \sum_{A}^{M}\frac{Z_A}{r_{1A}} \tag{2.32}$$

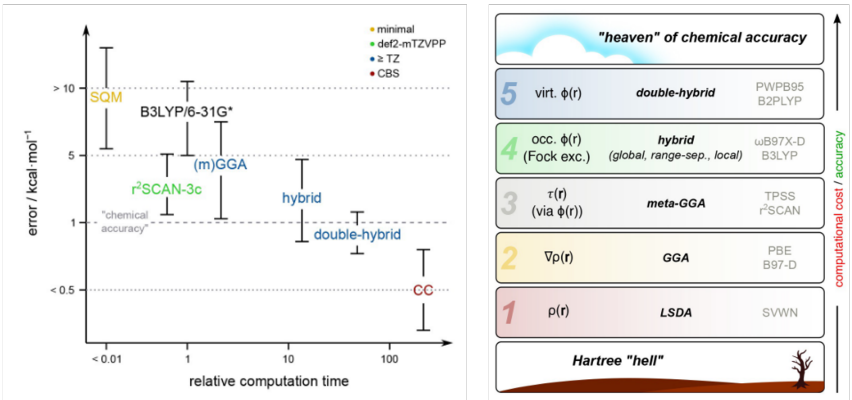

Figure 2.2: Left panel: accuracy of the common quantum chemical methods as a function of the computatinal cost. Right panel: categorisation of the exchange-correlation functionals according to Perdew's "Jacob's ladder". The figure was reproduced from [39].

The iterative procedure to solve these equations proceeds as follows: first, a trial electron density is defined. Then, the Kohn-Sham equations are solved using this trial density to obtain the single-particle wavefunctions. Next, a new electron density is calculated from the obtained wavefunctions. Finally, the new density is compared with the initial trial density. If the two densities match within a given convergence criterion, the ground state electron density has been found, and the total energy of the system can be computed.

2.2.2 Generalised gradient approximation and PBE functional

The field of DFT has opened new avenues for computational chemists and physicists, enabling them to study the properties of materials and molecules, as well as to investigate the reaction pathways of chemical processes. However, the accuracy of DFT calculations is highly dependent on the choice of the exchange-correlation functional.

In this work, we focus on the generalised gradient approximation (GGA) exchange-correlation functionals, which are widely used in DFT calculations and are known to provide results close to chemical accuracy at a relatively low computational cost, as can be seen in Figure 2.2. In fact, the development of GGA functionals marked a turning point in the acceptance of the DFT method by the quantum chemistry community.

The GGA functionals are based on the idea that the exchange-correlation energy can be expressed as a functional of the electron density ρ and its gradient $\nabla\rho$. The general form of a GGA functional is given by:

$$E_{\mathrm{XC}}^{\mathrm{GGA}}[\rho] = \int f(\rho, \nabla\rho)\, d\mathbf{r} \tag{2.33}$$

The exchange-correlation energy can be explicitly divided into two parts:

$$E_{XC}^{GGA} = E_{X}^{GGA} + E_{C}^{GGA} \tag{2.34}$$

One of the most widely used GGA functionals is the Perdew-Burke-Ernzerhof (PBE) functional [40]. Its formulation incorporates 4 parameters in the exchange and correlation parts derived from first principles, making it a truly *ab initio* functional.

2.2.3 *Ab initio* molecular dynamics

In one of the previous sections, we touched upon the topic of classical MD simulations. However, classical force fields are unable to simulate bond-breaking and bond-forming processes. Although reactive events can also be studied using static approaches, by calculating the potential energy surface at a given set of coordinates, we believe that incorporating dynamics provides more informative insights and a clearer picture of the reaction mechanism.

To simulate the dynamics of a chemical reaction, one could consider using *ab initio* molecular dynamics (AIMD), and in particular, Born-Oppenheimer molecular dynamics (BOMD). In BOMD, the forces acting on the atoms are calculated at each time step using quantum mechanical methods, such as DFT, while the nuclei are propagated according to classical mechanics. This process can be described using the Lagrangian formalism, L, which offers an alternative formulation of classical dynamics:

$$L = K - U = \frac{1}{2}\sum_{i=1}^{3N} m_i v_i^2 - E[\phi(\mathbf{r}_1, \ldots, \mathbf{r}_{3N})] \tag{2.35}$$

where K is the kinetic energy, U represents the potential energy, and $\phi(\mathbf{r}_1, \ldots, \mathbf{r}_{3N})$ is a set of one-electron Kohn-Sham wave functions.

It is important to note that, since nuclear dynamics are treated classically in this framework, zero-point vibrational energy is not accounted for, nor can tunnelling effects be studied.

2.3 Extended tight binding

The tight binding methods can be viewed as a simplification, or semi-empirical approximation, of DFT. Essentially, they are based on the same principles but introduce numerous approximations to reduce the computational cost. In 2017, the extended tight-binding (xTB) method was introduced. This development led to a new family of methods, namely GFNn-xTB, where GFN stands for geometries, frequencies, and non-covalent interactions, and *n* denotes the version [41].

In density functional tight-binding (DFTB) methods, the total energy of a system is expressed as a Taylor expansion around $\Delta\rho$ [42]:

$$E[\rho] = E^{(0)}[\rho_0] + E^{(1)}[\rho_0, \delta\rho] + E^{(2)}[\rho_0, (\delta\rho)^2] + E^{(3)}[\rho_0, (\delta\rho)^3] + \cdots \tag{2.36}$$

Here, $\Delta\rho$ represents the difference between the converged ρ and the reference density ρ_0. The terms represent zeroth-order (core-core repulsion), first-order (valence electronic energy), second-order (charge corrections), and higher-order terms [27]. GFNn-xTB is heavily based on DFTB3, which includes terms in the energy expansion up to third order. The energy of GFN1-xTB, which is considered in this work, is given by [42]:

$$\begin{aligned} E_{\text{GFN1-xTB}} &= E^{(0)}_{\text{rep}} + E^{(0)}_{\text{disp}} + E^{(0)}_{\text{XB}} + E^{(1)}_{\text{EHT}} + E^{(2)}_{\text{IES+IXC}} + E^{(3)}_{\text{IES+IXC}} \\ &= E_{\text{rep}} + E^{\text{D3}}_{\text{disp}} + E^{\text{GFN1}}_{\text{XB}} + E_{\text{EHT}} + E_{\gamma} + E^{\text{GFN1}}_{\Gamma} \end{aligned} \tag{2.37}$$

where E_{rep} is the repulsion energy, $E^{\text{D3}}_{\text{disp}}$ is the dispersion energy, $E^{\text{GFN1}}_{\text{XB}}$ is the exchange-bonding energy, E_{EHT} is the extended Hückel theory energy, and E_{γ} and E^{GFN1}_{Γ} correspond to contributions arising from density fluctuations.

It is important to note that the GFNn-xTB methods are parametrised for 86 elements using a partially polarised minimal valence basis set. GFN1-xTB provides a good first approximation of the potential energy surface and is computationally efficient, thus making it suitable for the initial exploration of large molecular systems and running relatively long MD simulations.

2.4 Neural network potentials

The discussion in this section is mainly based on the textbook “Deep Learning: Foundations and Concepts” by C. M. Bishop and H. Bishop [43], the excellent review by Duval, Mathis, Joshi, and Schmidt et al. [44], the research paper by Batatia and Batzner et al. [45], and the research paper by Batzner et al. [46], unless stated otherwise.

2.4.1 Graph neural networks

One can easily imagine how computationally expensive it would be to run AIMD simulations for a system containing hundreds of atoms. In recent years, the field of machine learning has made significant progress in addressing this challenge. In particular, the development of graph neural networks (GNNs) has enabled the design of neural network potentials (NNPs), which learn the potential energy surface of molecular systems and can replace DFT in molecular dynamics simulations.

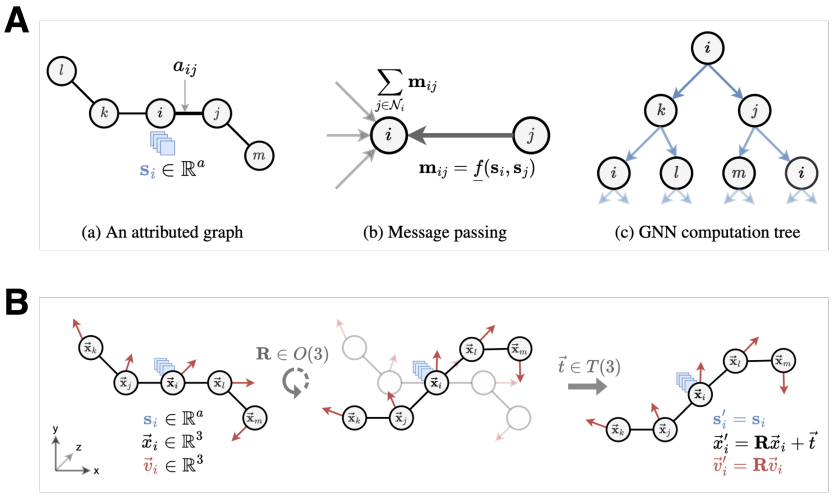

Figure 2.3: The concept of (A) GNNs and (B) geometric GNNs visualised. This figure was reproduced from [44].

A natural question one may ask here: why use GNNs? The answer lies in the fact that GNNs provide a natural way to represent molecular systems. Atoms can be considered as nodes in a graph, with bonds between them represented as edges. This concept is visualised in Figure 2.3 A.

An essential property of any graph $\mathcal{G} = (\mathbf{A}, \mathbf{S})$ is its adjacency matrix $\mathbf{A}$, which encodes the connectivity of the nodes via elements a_{ij}. This matrix is square with dimensions $n \times n$, where n is the number of nodes in the graph. Each entry is either 0 or 1, indicating the absence or presence of a connection between two nodes.

Because the ordering of nodes in the graph is arbitrary, GNNs are, by construction, permutation symmetric.

In addition to the adjacency matrix, each graph also has a matrix of scalar features $\mathbf{S}$ associated with its nodes. In the case of molecular systems, these features may include atomic numbers or atom types.

GNNs are neural networks specifically designed to operate on graph-structured data. They learn representations of nodes, edges, or entire graphs by iteratively updating node features based on their neighbours $\mathcal{N}_i$. This iterative process is commonly referred to as message passing, illustrated in Figure 2.3 A. Conceptually, the process proceeds as follows:

1. At iteration t, each node i receives messages from its neighbours $\mathcal{N}_i$:

$$\mathbf{m}_{ij}^{(t)} = \underline{\text{MSG}}\left(\mathbf{s}_i^{(t)}, \mathbf{s}_j^{(t)}\right) \tag{2.38}$$

2. These messages are aggregated to update the node's features: $\bigoplus_{j \in \mathcal{N}_i} \mathbf{m}_{ij}^{(t)}$.

3. At iteration $t+1$, the node's representation is updated using the aggregated messages and its current state:

$$\mathbf{s}_i^{(t+1)} = \underline{\text{UPD}}\left(\mathbf{s}_i^{(t)}, \bigoplus_{j \in \mathcal{N}_i} \mathbf{m}_{ij}^{(t)}\right) \tag{2.39}$$

The MSG and UPD functions form an entire research topic within GNNs, and are typically implemented as neural networks themselves. The aggregation operator $\bigoplus$ must be permutation-invariant and can take forms such as summation, averaging, etc. After the final iteration, the resulting node representations can be used to predict properties at various levels, whether for the entire graph, such as the total energy of a molecular system, or at the node or edge level.

A particularly important subclass of GNNs is the geometric GNNs, which are designed to handle geometric data in Euclidean space. These are depicted in Figure 2.3 B. Geometric graphs $\mathcal{G} = (\mathbf{A}, \mathbf{S}, \vec{\mathbf{x}}, \vec{\mathbf{v}})$ contain additional information such as atomic coordinates $\vec{x}_i$ and other vector features $\vec{v}_i$. These vectors may represent quantities such as velocities or forces.

Geometric GNNs are tailored to work with data that has an inherent geometric structure, such as point clouds. Their key advantage is in handling symmetry operations, i.e. that under rotations and translations of the data, scalar features remain invariant, or the same, while vector features transform appropriately. This property is crucial for accurately capturing the underlying physics of molecular systems.

2.4.2 Invariance and equivariance

In the context of geometric GNNs, the concepts of invariance and equivariance play a fundamental role in ensuring that models respect the symmetries of the data they are trained on. These properties are especially crucial when working with molecules, where rotations or translations should not change the outcome of the prediction or should change it in a predictable way.

Mathematically, a function f is said to be invariant to a transformation g if applying g to the input x does not affect the output of the function:

$$f(g \cdot x) = f(x) \tag{2.40}$$

A simple real-world example of invariance is the total energy of a molecule. Typically it stays invariant under rotations and translations of its atomic coordinates.

On the other hand, a function f is said to be equivariant to a transformation g if

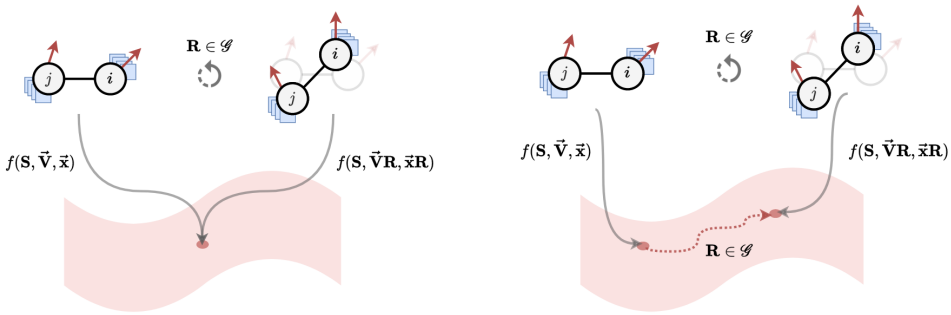

(a) $\mathcal{G}$-invariant function (b) $\mathcal{G}$-equivariant function

Figure 2.4: Invariance and equivariance. This figure was taken from [44].

applying g to the input results in the same transformation being applied to the output:

$$f(g \cdot x) = g \cdot f(x) \tag{2.41}$$

A familiar example of equivariance is the behaviour of vector quantities such as velocity or force. If we rotate a coordinate system (or the object within it), the velocity or force vectors will also rotate accordingly. In the context of molecular systems, atomic forces are equivariant under rotations: if the molecule is rotated, the directions of the forces rotate in the same way. Both concepts of invariance and equivariance are illustrated in Figure 2.4.

Designing GNNs that are invariant or equivariant helps reduce the amount of data needed for training. Geometric neural networks, for instance, are explicitly constructed to respect such symmetries, making them particularly well-suited for chemical modelling.

2.4.3 Equivariant graph neural networks

In the previous section, we emphasised the importance of implementing invariance and equivariance in GNNs. In general, the field of geometric GNNs applied to computational chemistry problems is still in its early stages, since the first models were introduced around 2018, as shown in Figure 2.5 A.

Nevertheless, the field is rapidly developing, with new architectures being proposed that advance the state of the art. These architectures achieve better performance in learning the intricacies of the potential energy surface while also scaling to systems containing millions of atoms [47].

In this section, we focus on the general pipeline of geometric GNNs, and on the NequIP [46] neural network in particular, which stands for Neural Equivariant Interatomic Potential. The general pipeline of geometric GNNs is shown in Figure 2.5 B.

Broadly speaking, the entire workflow can be divided into three main steps:

1. Create the atomic representations.
2. Learn the embeddings of the atomic representations.
3. Predict the desired output property, such as the total energy or forces.

Atomic representations

Before learning atomic representations, the network constructs an input graph from the given atomic coordinates, i.e., a point cloud. Atoms are treated as nodes, and edges are formed between atoms that lie within a specified cutoff radius. This radius defines the local environment of each atom and is crucial for ensuring that the network processes only physically meaningful interactions. To ensure a gradual change in interaction strength, a smooth cutoff function is often employed. It has the following form:

$$A_{ij} = \begin{cases} \frac{1}{2}\left(\cos\left(\frac{\pi d_{ij}}{c}\right) + 1\right) & \text{if } d_{ij} \leq c \\ 0 & \text{otherwise} \end{cases} \tag{2.42}$$

Here, $d_{ij} = ||\vec{x}_i - \vec{x}_j||$ is the distance between atoms i and j, and c is the cutoff radius. The cutoff function smoothly transitions from 1 to 0 as the distance approaches the cutoff, ensuring that interactions are considered only within the specified range. This function is typically chosen to be continuous and differentiable, such as a cosine or polynomial function, to avoid discontinuities. The choice of cutoff radius is critical, as it determines the size of the local environment considered by the network. A cutoff that is too small may lead to the loss of important long-range interactions, while one that is too large may introduce noise and increase computational cost.

When working with periodic systems, periodic boundary conditionss (PBCs) must be respected during graph construction. Therefore, adjacent unit cells are considered within the cutoff distance to ensure that atomic environments are correctly represented.

Alongside the geometric information, usually encoded as distance-based features, each atom is assigned a type-dependent feature, often implemented as an atomic embedding vector. In addition to pairwise distances, some architectures incorporate angular information or more complex symmetry functions to capture higher-order geometric correlations. Together, these inputs form the basis of the graph on which the neural network operates.

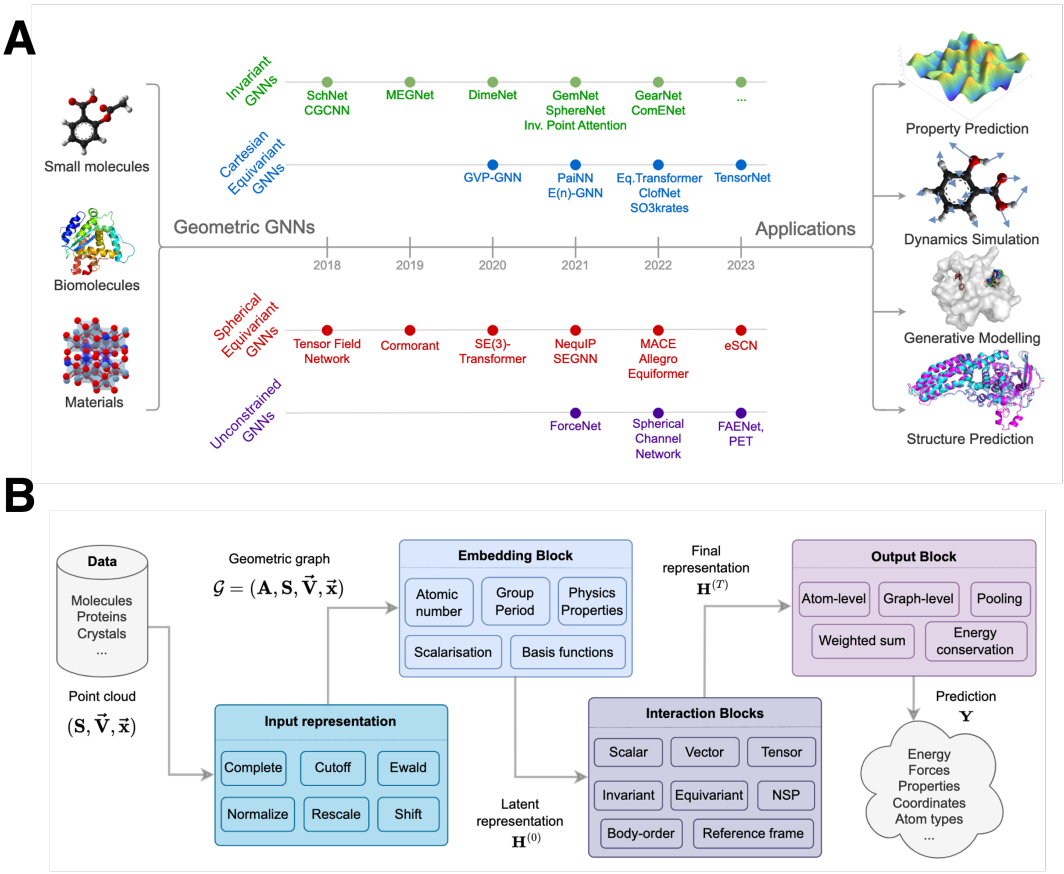

Figure 2.5: (A) The timeline of the development of geometric GNNs aimed at computational chemistry problems. (B) A general architecture of geometric GNNs. This figure was reproduced from [44].

Embedding and interaction blocks

Once the input features have been defined, the network proceeds through an initial embedding layer. This layer maps the input features into a latent space, which may consist of scalars, vectors, or higher-order tensors ℓ, depending on the network's level of geometric complexity. For instance, in NequIP, the input features are mapped into spherical tensors ℓ that are irreducible representations of $SO(3)$ thanks to the e3nn library [48], ensuring rotational equivariance, while translational invariance is built in by using relative positional features. In other words, the embedding layer constructs the initial learnable atomic representations that will be refined by the subsequent layers of the network.

The core of the network comprises a series of interaction, or message-passing, blocks. Within each block, nodes aggregate both scalar and vector information from their neighbours, often using edge features such as relative positions or spherical harmonics to guide the update. The aggregated messages are then passed through neural network layers. As a result, each node's feature vector is updated in a way that pre-

serves the geometric structure of the system. By stacking multiple interaction blocks, the network gains the capacity to capture complex many-body interactions. Each layer builds upon the features extracted by the previous one, allowing the model to learn increasingly rich representations of atomic environments.

Output block

The final stage of a geometric GNN involves translating the atomic representations, refined by the embedding and interaction blocks, into physically meaningful quantities, such as the total energy of the system. This quantity is typically obtained as a sum over per-atom contributions, a strategy that ensures permutation invariance with respect to atomic indexing.

To derive atomic forces, two main approaches can be used: either predicting them directly or utilising automatic differentiation. In the latter case, forces are computed as the negative gradient of the predicted energy with respect to atomic positions using automatic differentiation as implemented in modern deep learning libraries. This approach ensures that the forces are conservative and thus obey the fundamental law of energy conservation. Moreover, since the model is constructed to respect geometric symmetries, the resulting forces are also equivariant under rotations and translations.

Thanks to the incorporating the physics-inspired features and symmetry constraints, the output of the network provides physically meaningful predictions of both total energy and atomic forces.

Chapter 3

Computational details

This chapter provides detailed information on the computational methods employed in this work. The first section outlines the generation of the training dataset, including system preparation, initial equilibration using molecular mechanics, exploration of the configuration space at the GFN1-xTB level, further data labelling, and iterative training of the neural network potential. The second section discusses production runs at ambient temperature using the fitted neural network potential. Finally, the third section presents the data analysis and visualisation techniques used to interpret the results.

3.1 Training dataset generation

3.1.1 System preparation

The systems were prepared using the functionality of the CHARMM-GUI webserver [49], specifically the Multicomponent Assembler interface [50].

As a first step, methyl diphosphate trianion (MeDP) and methyl diphosphate dianion (MeHDP) were parameterised using CGenFF [51], i.e., the CHARMM General Force Field. These protonation states were chosen based on the dissociation constants of pyrophosphoric (diphosphoric) acid [52]:

$$\begin{aligned} H_4P_2O_7 &\rightleftharpoons [H_3P_2O_7]^- + H^+, \quad pK_a = 0.91 \\ [H_3P_2O_7]^- &\rightleftharpoons [H_2P_2O_7]^{2-} + H^+, \quad pK_a = 2.10 \\ [H_2P_2O_7]^{2-} &\rightleftharpoons [HP_2O_7]^{3-} + H^+, \quad pK_a = 6.70 \\ [HP_2O_7]^{3-} &\rightleftharpoons [P_2O_7]^{4-} + H^+, \quad pK_a = 9.32 \end{aligned}$$

Thus, at physiological pH (7.4), this acid exists in equilibrium between the singly and doubly deprotonated forms. Assuming the methyl group behaves similarly to a

proton, the methyl diphosphate molecule was considered to exist as a mixture of the MeHDP and MeDP forms under physiological conditions.

Following successful parameterisation, the system was solvated in a cubic box of TIP3P water molecules, with sodium counterions (Na^+) added to neutralise the system's overall charge. The final system composition is provided in Table 3.1.

3.1.2 Initial equilibration using classical force fields

The system equilibration followed the standard protocol generated by the CHARMM-GUI webserver [49]. Initially, energy minimisation was conducted using the steepest descent algorithm for 5,000 steps.

This was followed by equilibration in the constant number of particles, volume and temperature (NVT) ensemble for 5 ns. During both the minimisation and NVT phases, the solute's heavy atoms were restrained using a harmonic potential with a force constant of 400 kJ mol^{-1} nm^{-2}.

Subsequently, the system was equilibrated in the constant number of particles, pressure and temperature (NPT) ensemble for 45 ns. Throughout this procedure, the temperature and pressure were maintained at 300 K and 1 bar, respectively. Temperature was controlled using a ν-rescale thermostat [32] with a coupling constant of 1 ps, and pressure was regulated using an isotropic *c*-rescale barostat [53] with a coupling constant of 5 ps. A 0.6 nm cut-off was applied for non-bonded interactions, and long-range electrostatics were treated using the Particle Mesh Ewald (PME) method. PBC were applied in all directions throughout the simulation.

All simulations were carried out using GROMACS 2021.4 [54] with CHARMM36m force field [55]. The leap-frog integrator was employed with a time step of 1 fs. All hydrogen-involving bonds were constrained using the LINCS algorithm. The equilibrated box dimensions used for subsequent simulations were taken from the output of the NPT run and are summarised in Table 3.1. Unless otherwise stated, the last frame of the NPT simulations was used as the starting point for all further calculations.

Table 3.1: System composition and simulation box details.

System	Final box dimensions ($Å^3$)	No. of H_2O	No. of Na^+	No. of atoms
MeDP	$15.877 \times 15.877 \times 15.877$	119	3	373
MeHDP	$15.901 \times 15.901 \times 15.901$	124	2	388

3.1.3 Collective variables

To effectively sample the reaction space, two types of CVs were employed to bias the system: distances and coordination numbers (CNs). The CN is defined by the following smooth function:

$$\sum_{i\in A}\sum_{j\in B} CN_{ij} = \frac{1-\left(\frac{r_{ij}-d_0}{r_0}\right)^n}{1-\left(\frac{r_{ij}-d_0}{r_0}\right)^m} \tag{3.1}$$

where r_{ij} is the distance between atoms i and j from groups A and B, d_0 is the distance at which the CN begins to decay, r_0 is a characteristic decay length, and n and m are integers that control the steepness of the decay. Typically, $m > n$, ensuring a smooth transition of CN_{ij} from approximately 1 to 0 as the distance increases.

The specific CVs used in this work are shown in Figure 3.1, and their corresponding parameters are as follows:

- Distance between the β-phosphorus and the bridging oxygen ($d_{P\text{-}O_{lg}}$),
- Coordination number of all water oxygen atoms as well as the bridging oxygen surrounding the β-phosphorus ($C_{P\text{-}O_{all}}$): $d_0 = 0$, $r_0 = 2.1$ Å, $n = 8$, $m = 16$.

Additionally, the following CVs were monitored to check whether the system was in a reasonable region of the potential energy surface, e.g. to ensure that there is no oxygen exchange between the methyl diphosphate and the water molecules:

- Coordination number of 3 nonbridging phosphoryl oxygens surrounding the β-phosphorus ($C_{P\text{-}O_{nb}}$): $d_0 = 0$, $r_0 = 2.1$ Å, $n = 8$, $m = 16$,
- Coordination number of 2 nonbridging oxygens from α-phosphorus as well as the one forming a bond with the methyl group surrounding the β-phosphorus ($C_{P\text{-}O_{nb\text{-}lg}}$): $d_0 = 0$, $r_0 = 2.1$ Å, $n = 8$, $m = 16$,

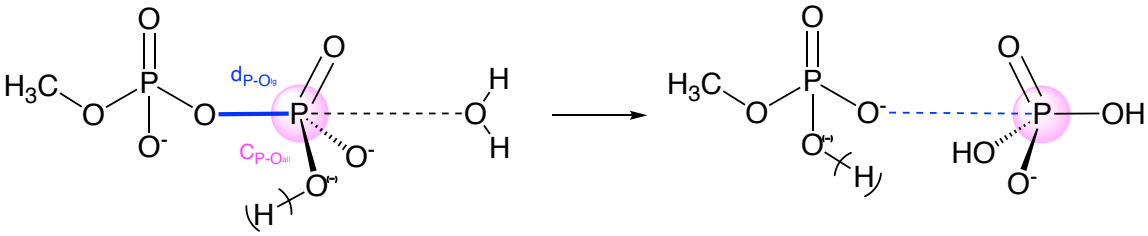

$d_{P\text{-}O_{lg}}$ = d(P - O_{lg}), $C_{P\text{-}O_{all}}$ = CN(P - O_{all})

Figure 3.1: The definition of the collective variables (CVs) used in this work. d stands for distance and CN stands for coordination number.

- Coordination number of water oxygens around the β-phosphorus ($C_{P\text{-}O_w}$): $d_0 = 0$, $r_0 = 2.1$ Å, $n = 8$, $m = 16$,
- Coordination number of non-methyl hydrogen atoms around 5 non-bridging and 1 bridging oxygen atoms ($C_{O\text{-}H_{all}}$): $d_0 = 0$, $r_0 = 1.3$ Å, $n = 8$, $m = 16$.

To avoid sampling of unphysical regions of the potential energy surface, quadratic (harmonic-like) wall potentials were applied to softly constrain certain degrees of freedom. The mathematical form of these wall potentials is given below:

$$\text{For upper walls: } \sum_i k_i \left(\frac{CV_i - a_i + o_i}{s_i} \right)^{e_i} \tag{3.2}$$

$$\text{For lower walls: } \sum_i k_i \left| \frac{CV_i - a_i - o_i}{s_i} \right|^{e_i} \tag{3.3}$$

Here, CV_i denotes the value of the collective variable, k_i is the force constant defining the wall's strength, a_i is the central wall position, o_i is an offset, s_i is a scaling factor, and e_i is the exponent that controls the wall's steepness. When $e_i = 2$, the potential acts harmonically.

The wall potentials applied to the CVs during the simulations are summarised in Table 3.2. The parameters for the wall potentials were chosen based on the expected ranges of the CVs. The force constants were set to ensure that the walls were sufficiently strong to prevent unphysical configurations while allowing for reasonable exploration of the configuration space.

All CV-related computations were performed using the built-in tools of CP2K 2023.1 [56] or PLUMED 2.9.3 [57]. It is important to note that the number and type of CVs, as well as the applied restraints, varied depending on the specific stage of the workflow. In the following sections, the relevant collective variables and wall potentials will be specified accordingly.

Table 3.2: The restraints applied to the collective variables during some of the simulations. In all cases, $o = 0$, $s = 1$, $e = 2$. [1]During the iterative training / production runs. [2]Different values for the walls were used depending on the system MeDP/MeHDP. Distances are in Å and coordination numbers are unitless.

CV	Lower wall	Upper wall	Force constant (kcal mol^{-1} Å^{-2})
$d_{P\text{-}O_{lg}}$	–	5.0 / 6.0[1]	500
$C_{O\text{-}H_{all}}$	–	1.3 / 2.5[2]	1000
$C_{P\text{-}O_{nb}}$	2.6	–	2000
$C_{P\text{-}O_{nb\text{-}lg}}$	–	– / 0.1[1]	2000
$C_{P\text{-}O_w}$	–	1.3	2000

3.1.4 GFN1-xTB based exploration of the configuration space

To generate the initial set of configurations for the training dataset, the system was subjected to molecular dynamics simulations using the semi-empirical GFN1-xTB [41] level of theory.

Each system was first equilibrated for 5 ps in the NVT ensemble at 300 K to allow the structures to relax at the GFN1-xTB level, including a Grimme's D3 dispersion correction [58]. Following equilibration, we performed 50 ps of WTMetaD [35] simulations in the NVT ensemble. In these simulations, a biasing potential was applied to encourage the system to explore regions of the configuration space beyond the reactant basin. This bias was introduced along two CVs: the distance between the β-phosphorus and the oxygen atom connecting it to the rest of the molecule ($d_{P\text{-}O}$), and the coordination number of all water oxygens together with the bridging oxygen surrounding the β-phosphorus atom ($C_{P\text{-}O}$). No restraints were applied to the system during this stage.

All calculations were carried out using the CP2K 2023.1 package [56] on CPUs. Temperature control was achieved using the CSVR thermostat [32], with a time constant of 50 fs during equilibration and 100 fs during the WTMetaD simulations. The self-consistent field (SCF) convergence threshold was set to 10^{-5} a.u. The biasing potential was updated every 25 fs, with a Gaussian hill height of 2 kcal mol^{-1} and a width of 0.07 for each CV. The bias factor was set to 30. Finally, the integration time step was set to 0.5 fs. Throughout the simulations, PBC were applied in all directions.

3.1.5 Data labeling

All data points were labeled by performing single-point calculations to obtain the energy and force values. These single-point calculations were carried out using the Perdew-Burke-Ernzerhof exchange-correlation functional (PBE) [40], along with a Grimme's D3 dispersion correction and the Becke-Johnson damping function [58, 59]. In all calculations, the Goedecker-Teter-Hutter pseudopotentials (GTH) [60, 61] were used to represent the core electrons, in combination with the triple-ζ valence basis set with two polarisation functions (TZV2P).

The single-point calculations were performed using the Gaussian plane wave method (GPW) implemented in the QUICKSTEP module [62] of the CP2K 2023.1 package [56]. The SCF convergence threshold was set to 10^{-6} a.u. A plane-wave cutoff of 800 Ry was applied for the total density, while a cutoff of 60 Ry was used for the Kohn-Sham orbitals.

The aforementioned cutoffs were determined based on a convergence test performed on one of the configurations, as described in [63]. An error in total energy of

less than 10^{-8} a.u. was considered acceptable for the convergence test. The test was conducted by varying the cutoff for the total density from 400 to 1500 Ry, and the cutoff for the Kohn-Sham orbitals from 10 to 200 Ry. The results of the convergence test are shown in Table A.1.

After the DFT labelling, the data were transformed into the extended XYZ format, which includes atomic positions, forces, total energies, cell dimensions, and whether PBC were used or not. This format was chosen because it is compatible with neural network training, as explained in the next section. The data transformation was carried out using an in-house script, `cp2k2extxyz.py`, which is available in [64].

3.1.6 Iterative training of the neural network potential

We trained a NNP using the NequIP framework [46], which implements equivariant message-passing networks for atomistic simulations. Regarding the hyperparameters, a radial cutoff distance of 5.0 Å was chosen to describe the atomic environment of the system.

The equivariant part of the neural network was composed of four interaction layers with a maximum tensor rank of $\ell = 1$ or 2. Feature parity was enabled to include both even and odd components, and 32 features per irreducible representation were used throughout. Scalar and gating nonlinearities were set to `silu` and `tanh` for even and odd parities, respectively. Eight radial basis functions were employed, in combination with a trainable Bessel basis and a polynomial cutoff of order 6.

The invariant subnetwork for radial interaction modelling consisted of two layers with 64 hidden neurons. Self-connections were enabled, and the average number of neighbours was computed automatically based on the dataset.

Training was performed using the Adam optimizer with the AMSGrad variant enabled, and with $\beta_1 = 0.9$, $\beta_2 = 0.999$, and $\epsilon = 10^{-8}$. A starting learning rate of 0.01 was used, and the learning rate was adaptively reduced by a factor of 0.5 upon stagnation of the validation loss (patience = 100 epochs). Early stopping was triggered if the validation loss remained unimproved for 50 epochs, if the loss dropped below 1×10^{-5}, or if it exceeded 1×10^{4}. The batch size was set to 5. The training was carried out over a period of three days on a single NVIDIA A100 GPU using float64 precision.

The networks were trained using the following mean squared error (MSE) loss function already implemented in the NequIP framework:

$$\mathcal{L} = \lambda_E \|\hat{E} - E\|^2 + \lambda_F \frac{1}{3N} \sum_{i=1}^{N} \sum_{\alpha=1}^{3} \left\| -\frac{\partial \hat{E}}{\partial r_{i,\alpha}} - F_{i,\alpha} \right\|^2 \tag{3.4}$$

Here, N is the number of atoms, $\hat{E}$ is the predicted energy, E is the reference

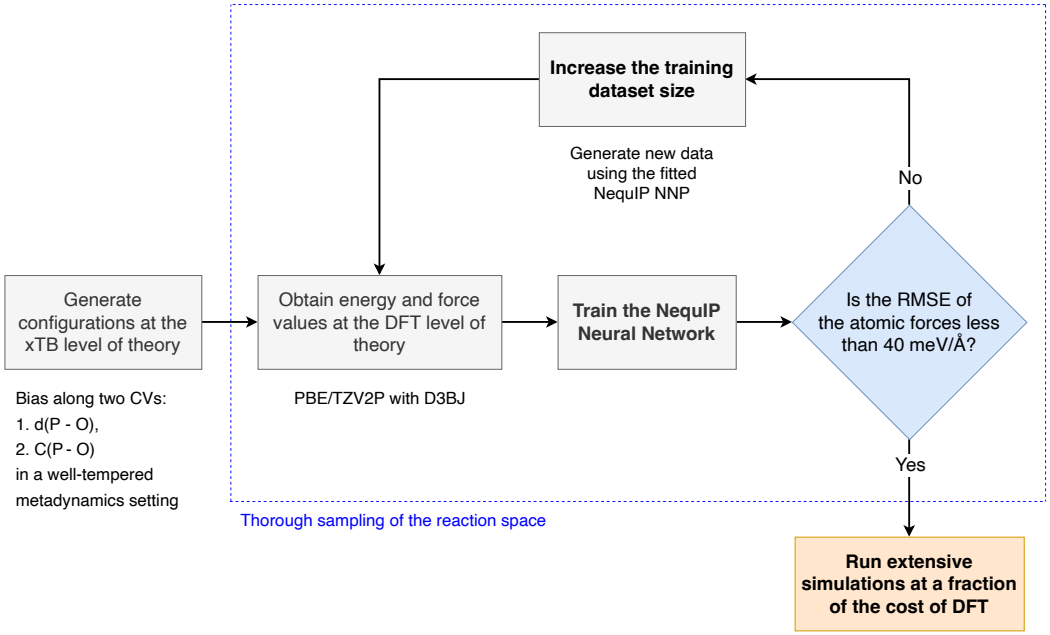

Figure 3.2: Iterative training of the NequIP neural network potential.

energy, $F_{i,\alpha}$ is the reference force on atom i in direction α, and $-\frac{\partial \hat{E}}{\partial r_{i,\alpha}}$ is the calculated force by means of autodifferentiating the predicted energy with respect to the atomic position. The hyperparameters λ_E and λ_F by default have a weighting of 1 to N_{atoms}^2, respectively.

To thoroughly sample the reaction space, the training was performed in an iterative manner, where the model was first trained on a small set of data and then used to generate additional data points. This process was repeated until the model converged, with the root mean square error (RMSE) of the atomic forces being less than 40 meV/Å. The workflow is shown in Figure 3.2.

In the end, the full dataset consisted of 12,000 configurations for training and validation, and 1,800 configurations for testing, for both systems (MeDP and MeHDP) combined. This dataset was obtained within the three rounds of iterative training. In each round of training, the model was retrained on a larger dataset. The data obtained from each round will be discussed in the following sections.

Selection of configurations for training and testing

An important part of the iterative training process is the selection of configurations that will be used to train the neural network. To construct a representative and diverse

dataset for training the neural network potential, configurations were selected from a metadynamics trajectory using a density-aware sampling strategy. The raw data were extracted from a file generated during the enhanced sampling simulations. Each configuration in this file corresponds to a simulation snapshot, annotated with a time index and two collective variables (CVs): the distance $d_{P\text{-}O_{lg}}$ and the coordination number $C_{P\text{-}O_{all}}$.

The two CVs were combined into a two-dimensional feature space $\mathbf{X} = (d, C)$, which served as the basis for sampling. This feature space often exhibits regions of highly non-uniform data density, due to the biased nature of metadynamics sampling. To account for this, a density-aware sampling method was employed to select configurations for training and testing that maintain good coverage across the feature space.

The selection procedure proceeds as follows:

1. A user-defined number of samples is specified.

2. K-means clustering is applied to the feature space to partition it into a number of clusters, k. The number of clusters is determined heuristically as $k = \max\left(10,\ \min\left(\left\lfloor \frac{N}{50} \right\rfloor, \left\lfloor \frac{n_{\text{samples}}}{10} \right\rfloor\right)\right)$, where N is the total number of configurations and n_{samples} is the desired number of samples.

3. The number of points sampled from each cluster is proportional to its size, ensuring that denser regions do not dominate the dataset. A minimum of one sample is taken from each non-empty cluster.

4. Within each cluster, a fixed number of configurations is randomly selected using a deterministic random seed to ensure reproducibility.

5. After the training set is selected, the remaining configurations are used to construct the test set, following the same density-aware procedure while ensuring no overlap with the training configurations.

This approach results in training and test datasets that closely mirror the overall distribution of the CVs, while ensuring that underrepresented regions of the feature space are adequately sampled. The final output consists of two lists of snapshot indices corresponding to the selected training and test configurations, along with their respective CV values. These snapshots were then extracted from the trajectory files for use in model training and evaluation. The pseudo-code for the density-aware sampling algorithm is provided in Algorithm A.1.

First round

In the first round of training the NNP, the model was trained on a small dataset consisting of 4,000 configurations. These configurations were obtained from the initial exploration of the configuration space at 300 K using the GFN1-xTB level of theory, as described in Section 3.1.4. The enhanced sampling simulations were biased along $d_{P\text{-}O_{lg}}$ and $C_{P\text{-}O_{all}}$, and no restraints were applied to the system. The training was carried out using the hyperparameters described in Section 3.1.6.

Second round

In the second round of training, the model was trained on a larger dataset consisting of 8,000 configurations. The additional configurations were obtained from a second round of exploration of the configuration space, driven by the NNP obtained after the first round of training.

The NNP-driven simulations were run using the LAMMPS package [65] compiled with PLUMED 2.9.3 [57] and `pair_nequip` [66] on a single A100 GPU. The simulations were performed for 100 ps in the NVT ensemble at 300 K with the PBC applied in all directions. The temperature was controlled by a Nosé–Hoover thermostat [30, 31] with a time constant of 50 fs. The biasing potential was applied to $d_{P\text{-}O_{lg}}$ and $C_{P\text{-}O_{all}}$ every 50 fs, using a Gaussian hill height of 2 kcal mol^{-1} and a width of 0.07 for each CV. The bias factor was set to 30, and the integration time step was 0.5 fs.

Restraints were applied to $d_{P\text{-}O_{lg}}$ and $C_{P\text{-}O_{all}}$ in order to favour either a dissociative or associative mechanism of the reaction and sample more configurations from the transition state (TS) regions. The training was performed using the same hyperparameters as in the first round.

Third round

In the final round of training, the model was trained on a dataset consisting of 12,000 configurations. These additional configurations were obtained from a third round of exploration of the configuration space, driven by the NNP obtained after the second round of training. The simulations were performed for 500 ps using the same setup as in the second round. The only difference was that the temperature in this round was increased to 320 K and 340 K to explore the configuration space at higher temperatures. The same CVs were biased as in the previous run. No restraints were applied to the system. The training was conducted using the same hyperparameters as in the first round. The final dataset is summarised in Table A.2.

3.2 Production runs at ambient temperature

To thoroughly sample the reaction space, the long production runs were performed at ambient temperature (300 K) using the neural network potential obtained in the final round of training. To run the simulations with the NNP, the LAMMPS package [65], compiled with PLUMED 2.9.3 [57] and `pair_nequip` [66], was utilised. First, the systems were equilibrated for 75 ps in NVT ensemble, since it was previously shown that water fully relaxes in this timeframe [67]. Then the simulations were carried out for 2 ns in the NVT ensemble, with temperature regulated by a Nosé–Hoover thermostat [30, 31] with a frequency of 50 fs^{-1}.

The biasing potential was applied every 50 fs to $d_{P\text{-}O_{lg}}$ and $C_{P\text{-}O_{all}}$ using a Gaussian hill height of 0.5 kcal mol^{-1} and a width of 0.07 for each collective variable. Additionally, restraints were imposed on the CVs as mentioned in Table 3.2. The bias factor was set to 30, and the integration time step was maintained at 0.5 fs. All simulations were conducted on a single A100 GPU.

To obtain the free energy profiles of the reactions, the Gaussian kernels applied during the simulations were summed using the `sum_hills` utility provided in the PLUMED 2.9.3 package [57]. Afterwards, the minimum free energy paths (MFEPs) were extracted using the MEPSA 1.4 software [68].

3.3 Data analysis and visualisation

Data analysis was performed using Python in Jupyter notebooks [69]. All plots were generated using Matplotlib library [70]. The water oxygen-oxygen $g_{O-O}(r)$ radial distribution function (RDF) was calculated using the extension in VMD [71] with the bin size of 0.0125 Å using the 2 ns of the production runs.

Chapter 4

Results and discussion

4.1 Final dataset composition

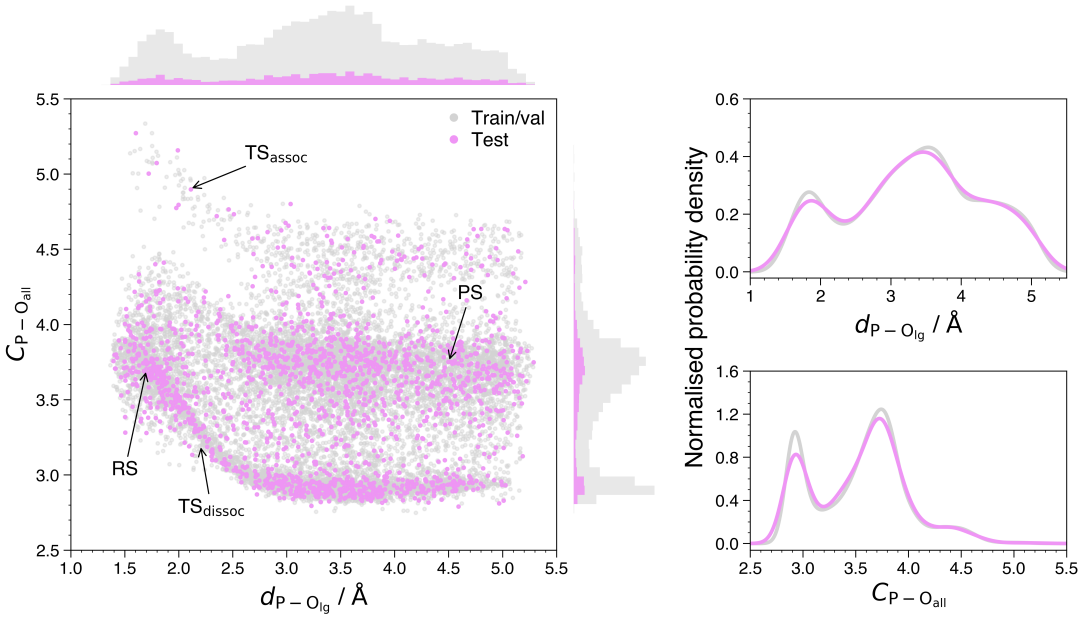

Figure 4.1: Left panel: final dataset composition projected on the two CVs space. RS stands for the reactant state, PS for the product state, and TS for the transition state. 50 bins were used to produce the histograms. Right panel: normalised densities of the two CVs for the training/validation and test sets.

The final dataset was obtained after three iterations of a learning loop, as described in Section 3.1.6. During each iteration, the dataset was expanded by adding points from different regions of the free energy surface (FES). This was achieved by imposing constraints on the CVs. For instance, in the first iteration, sampling primarily targeted the reactant and product basins, while in the second iteration, the focus shifted towards the transition state regions. The final iteration was dedicated to exploring the FES at

elevated temperatures (e.g., 320 and 340 K) in order to enhance the configurational diversity of the dataset. Sampling at higher temperatures generally improves the CV space coverage, as it allows the system to visit higher-energy regions.

The final dataset comprises 12,000 data points for the training and validation sets, and 1,800 points for the test set, as illustrated in the left panel of Figure 4.1.

The reactant basin is well-defined, appearing as a narrow region in the CV space. In contrast, the product basin is broader due to the diffusion of products within the simulation cell.

The sampling quality of the TS regions varies. The dissociative pathway is substantially better represented than the associative one. This difference arises from the fact that the associative path lies higher in energy and is therefore more difficult to access. Nevertheless, it is still represented by a number of points, meaning the fitted potential should be capable of describing it to some extent.

A particularly important aspect of dataset construction was the implementation of density-aware sampling. This approach was adopted for several reasons. First and foremost, the algorithm was used to ensure that the dataset is balanced in terms of the CVs distribution, as shown in the right panel of Figure 4.1. Secondly, it was employed to guarantee sufficient configurational diversity, i.e., the inclusion of points from various physically meaningful regions of the FES, thereby enhancing the potential's ability to generalise. This is crucial, as the neural network potential must be capable of predicting energies and forces for any configuration along the reaction coordinate. Lastly, density-aware sampling was used to ensure that the test set reflects the overall reaction space well, thereby providing a reliable basis for critically evaluating the accuracy and performance of the trained potential.

4.2 Accuracy and performance of the neural network potential

At each iteration, the potential was fitted using a NequIP equivariant GNN with a different tensor rank ℓ, namely $\ell = 1$ and $\ell = 2$ ($\ell = 0$ would correspond to an invariant GNN). The reason for using different tensor ranks was to investigate how the network complexity affects the accuracy of the potential. The tensor rank ℓ determines the number of parameters in the network, with higher values leading to more complex node representations.

The final potential was trained on 12,000 data points, and its accuracy is illustrated in Figure 4.2. The left panel shows the errors in the forces and energy for tensor rank $\ell = 1$, while the right panel shows the corresponding errors for $\ell = 2$. The errors are

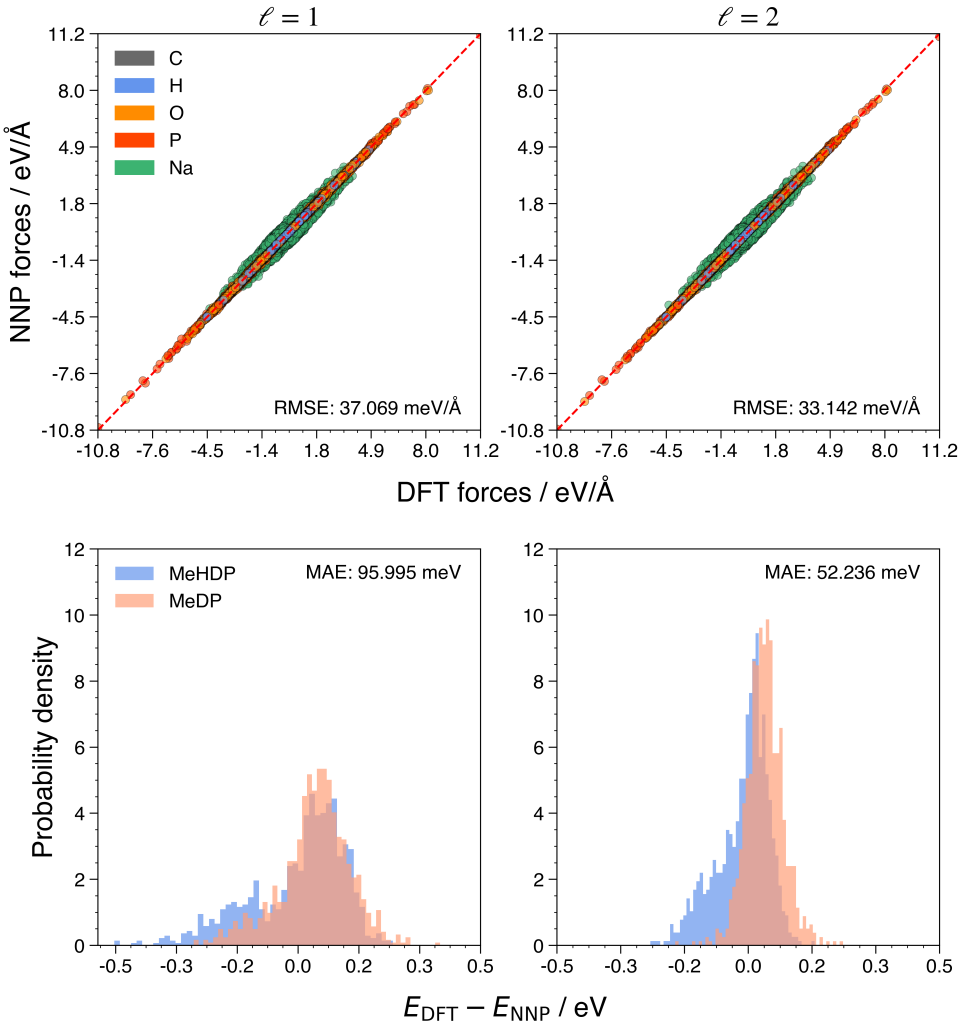

Figure 4.2: Accuracy of the neural network potential trained on 12,000 data points. The left panel shows the errors in the forces and energy for the tensor rank $\ell = 1$, and the right panel shows the errors for $\ell = 2$. For the histograms, the number of bins was set to 50.

calculated as the difference between the neural network potential and the reference DFT values.

According to current community standards [72], the accuracy of a neural network potential is considered a 'very good fit' when the RMSE in the forces lies within the range of 20-40 meV/Å and the mean absolute error (MAE) in the energy is between 1-10 meV/atom. A 'very accurate fit' is defined as the RMSE in the forces of approximately 10 meV/Å and the MAE in the energy on the order of 1 meV/atom.

The NNPs obtained in this work fall somewhere in between these two categories. The RMSE in the forces is 37.069 meV/Å for $\ell = 1$ and 33.142 meV/Å for $\ell = 2$, while the MAE in the energy is below 0.3 meV/atom for $\ell = 1$ and below 0.15 meV/atom for $\ell = 2$.

As shown in Figure 4.2, the errors in the forces lie along the diagonal, which rep-

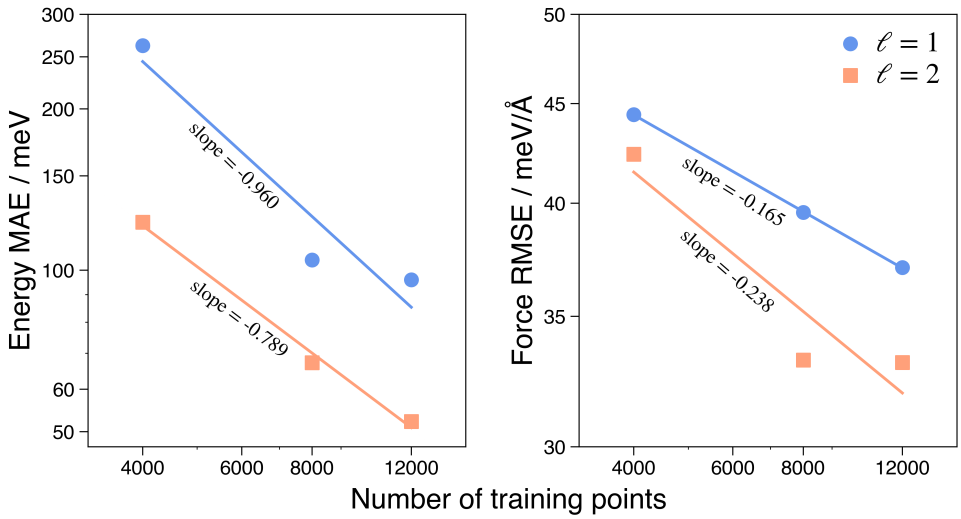

Figure 4.3: Log-log plot of the errors in the energy and forces for the neural network potential with respect to the training dataset size. In all cases, the errors were calculated on the final test set of 1,800 data points.

resents a perfect fit. The only points that are slightly scattered correspond to sodium cations (Na^+) jiggling in solution, not being technically bound to anything. This makes it more challenging for the network to predict the forces on them.

Regarding the energy predictions, the potential with $\ell = 1$ slightly overestimates them. This can be seen from the tail of the probability density on the left-hand side. The error appears to be systematic, meaning that when the NNP encounters new points close to those in the training data, it would produce a consistent error that may cancel out when evaluating energy differences. In contrast, the potential with $\ell = 2$ shows normally distributed energy errors, with no significant outliers. The histograms of the errors also demonstrate that the distributions are centred around zero, indicating that the potential does not systematically over- or under-estimate the energies and forces.

Overall, both potentials are very accurate, especially considering that they were trained on a fairly small dataset of 12,000 data points. This fact supports the idea that equivariant GNNs are indeed data-efficient. For instance, a related study [73] investigated phosphoester bond formation between orthophosphate and methanol in bulk water. In that case, to achieve force errors on the order of 50 meV/Å/atom, the authors had to train an invariant neural network, DeePMD [74], on 220,000-400,000 data points.

It is important to note that the potentials are only as accurate as can be assessed by the test set, which contains 1,800 points spanning the entire FES of the reaction. The test set was not used during training nor clashes with the training points, which confirms that the NNP generalises well to unseen data.

The generalisability of the potentials can be further assessed by analysing how the

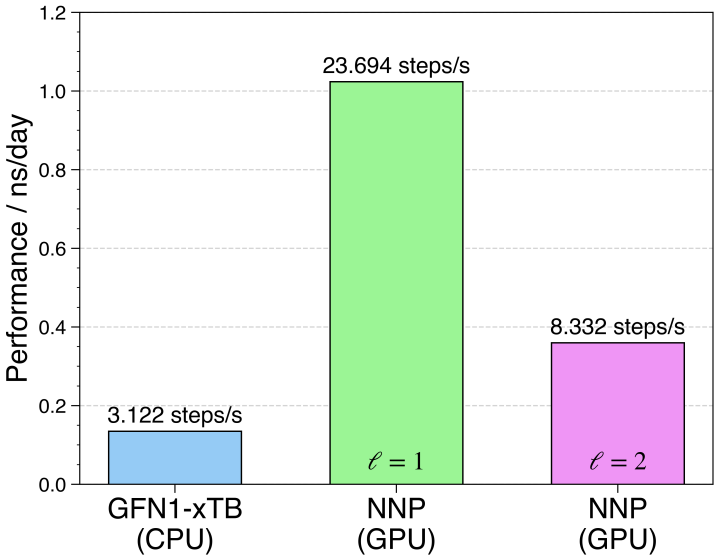

Figure 4.4: Comparison of the performance between the *ab initio* molecular dynamics runs driven by GFN1-xTB and neural network potentials fitted with different tensor ranks. CPU = 2 Intel Xeon Platinum 8468 CPUs (Sapphire Rapids), 48 cores each. GPU = 1 NVIDIA A100 80 GB GPU.

errors in the energy and forces vary with the training dataset size. Figure 4.3 shows a log-log plot of these errors for the NNP at each iteration of the learning loop. The errors were evaluated *a posteriori* on the final test set of 1,800 data points.

By examining the slopes, it becomes evident that the dataset size significantly influences how well the network learns the energies. The errors in the forces, however, are less sensitive to dataset size, which is reasonable given that the forces are not predicted directly by the network, but rather computed as the derivative of the energy with respect to atomic positions. Interestingly, the NNPs began producing sufficiently accurate results after the second training round, i.e., with 8,000 data points. This suggests that a dataset of 12,000 points is indeed sufficient to achieve a very good fit.

The next question to address is which of the two NNPs should be used in subsequent calculations. To answer this, the performance of the potentials was compared in terms of computational time required to run AIMD simulations. The results are presented in Figure 4.4. The AIMD simulations were performed on the MeDP system.

It is clear that the NNP with ℓ = 1 is significantly more efficient than both the ℓ = 2 NNP and GFN1-xTB. It is important to highlight that the number of trainable parameters in the ℓ = 1 NNP is 206,520, whereas for ℓ = 2 it is 452,280, making the latter nearly twice as slow in evaluating energies and gradients. Most likely, the performance of the PBE functional would be considerably slower - so much so that its bar would not appear on the plot.

Taking both accuracy and performance into account, the NNP with ℓ = 1 was se-

lected for further calculations. It is sufficiently accurate to describe the reaction mechanism, and fast enough to allow for extended AIMD simulations. The NNP with $\ell = 2$ could be used in future work if an even more accurate potential is required.

4.3 Stability of the production runs

4.4 Radial distribution function of water

4.5 Convergence of the free energy profiles

4.6 Evolution of the collective variables over time

4.7 Reaction mechanism for methyl diphosphate trianion

4.7.1 Minimum free energy path

4.7.2 Proton transfer mechanism

4.8 Reaction mechanism for methyl diphosphate dianion

4.8.1 Minimum free energy path

4.8.2 Proton transfer mechanism

Chapter 5

Conclusions and outlook

Bibliography

[1] Westheimer, F. H. Why Nature Chose Phosphates. *Science* **235**, 1173–1178 (1987).

[2] Wolfenden, R. Degrees of Difficulty of Water-Consuming Reactions in the Absence of Enzymes. *Chemical Reviews* **106**, 3379–3396 (2006).

[3] Müller, W. E., Schröder, H. C. & Wang, X. Inorganic Polyphosphates As Storage for and Generator of Metabolic Energy in the Extracellular Matrix. *Chemical Reviews* **119**, 12337–12374 (2019).

[4] Nebesnaya, K. S. *et al.* Inorganic polyphosphate regulates functions of thymocytes via activation of P2X purinoreceptors. *Biochimica et Biophysica Acta (BBA) - General Subjects* **1868**, 130523 (2024).

[5] Kamerlin, S. C. L., Sharma, P. K., Prasad, R. B. & Warshel, A. Why nature really chose phosphate. *Quarterly Reviews of Biophysics* **46**, 1–132 (2013).

[6] Pavlov, E. *et al.* Inorganic Polyphosphate and Energy Metabolism in Mammalian Cells *. *Journal of Biological Chemistry* **285**, 9420–9428 (2010).

[7] Dzeja, P. P. & Terzic, A. Phosphotransfer networks and cellular energetics. *Journal of Experimental Biology* **206**, 2039–2047 (2003).

[8] Boyer, P. D. Energy, Life, and ATP (Nobel Lecture). *Angewandte Chemie International Edition* **37**, 2296–2307 (1998).

[9] Bonora, M. *et al.* ATP synthesis and storage. *Purinergic Signalling* **8**, 343–357 (2012).

[10] Walker, J. E. The ATP synthase: The understood, the uncertain and the unknown. *Biochemical Society Transactions* **41**, 1–16 (2013).

[11] Baev, A. Y. & Abramov, A. Y. Inorganic Polyphosphate and F0F1-ATP Synthase of Mammalian Mitochondria. In Müller, W. E. G., Schröder, H. C., Suess, P. & Wang, X. (eds.) *Inorganic Polyphosphates: From Basic Research to Medical Application*, 1–13 (Springer International Publishing, Cham, 2022).

[12] Baev, A. Y., Angelova, P. R. & Abramov, A. Y. Inorganic polyphosphate is produced and hydrolyzed in F0F1-ATP synthase of mammalian mitochondria. *Biochemical Journal* **477**, 1515–1524 (2020).

[13] Walker, J. E. ATP Synthesis by Rotary Catalysis (Nobel lecture). *Angewandte Chemie International Edition* **37**, 2308–2319 (1998).

[14] Watt, I. N., Montgomery, M. G., Runswick, M. J., Leslie, A. G. W. & Walker, J. E. Bioenergetic cost of making an adenosine triphosphate molecule in animal mitochondria. *Proceedings of the National Academy of Sciences* **107**, 16823–16827 (2010).

[15] Kamerlin, S. C. L., Florián, J. & Warshel, A. Associative Versus Dissociative Mechanisms of Phosphate Monoester Hydrolysis: On the Interpretation of Activation Entropies. *ChemPhysChem* **9**, 1767–1773 (2008).

[16] Klähn, M., Rosta, E. & Warshel, A. On the Mechanism of Hydrolysis of Phosphate Monoesters Dianions in Solutions and Proteins. *Journal of the American Chemical Society* **128**, 15310–15323 (2006).

[17] Duarte, F., Åqvist, J., Williams, N. H. & Kamerlin, S. C. L. Resolving Apparent Conflicts between Theoretical and Experimental Models of Phosphate Monoester Hydrolysis. *Journal of the American Chemical Society* **137**, 1081–1093 (2015).

[18] Hassan, H. A., Rani, S., Fatima, T., Kiani, F. A. & Fischer, S. Effect of protonation on the mechanism of phosphate monoester hydrolysis and comparison with the hydrolysis of nucleoside triphosphate in biomolecular motors. *Biophysical Chemistry* **230**, 27–35 (2017).

[19] Prasad, B. R., Plotnikov, N. V. & Warshel, A. Addressing Open Questions about Phosphate Hydrolysis Pathways by Careful Free Energy Mapping. *The Journal of Physical Chemistry B* **117**, 153–163 (2013).

[20] Akola, J. & Jones, R. O. ATP Hydrolysis in Water - A Density Functional Study. *The Journal of Physical Chemistry B* **107**, 11774–11783 (2003).

[21] Glaves, R., Mathias, G. & Marx, D. Mechanistic Insights into the Hydrolysis of a Nucleoside Triphosphate Model in Neutral and Acidic Solution. *Journal of the American Chemical Society* **134**, 6995–7000 (2012).

[22] Wang, C., Huang, W. & Liao, J.-L. QM/MM Investigation of ATP Hydrolysis in Aqueous Solution. *The Journal of Physical Chemistry B* **119**, 3720–3726 (2015).

[23] Harrison, C. B. & Schulten, K. Quantum and Classical Dynamics Simulations of ATP Hydrolysis in Solution. *Journal of Chemical Theory and Computation* **8**, 2328–2335 (2012).

[24] Ramirez, F., Marecek, J. F. & Szamosi, J. Magnesium and calcium ion effects on hydrolysis rates of adenosine 5'-triphosphate. *The Journal of Organic Chemistry* **45**, 4748–4752 (1980).

[25] Ramirez, F., , M., James F. & and Szamosi, J. A Comparative Study of Hydrolysis Rates of 2′-Deoxyadenosine and Adenosine 5′-Triphosphates and 5′-Diphosphates. *Phosphorus and Sulfur and the Related Elements* **13**, 249–257 (1982).

[26] Dirac, P. A. M. & Fowler, R. H. Quantum mechanics of many-electron systems. *Proceedings of the Royal Society of London. Series A, Containing Papers of a Mathematical and Physical Character* **123**, 714–733 (1997).

[27] Jensen, F. *Introduction to Computational Chemistry* (John Wiley & Sons, 2017).

[28] Tuckerman, M. E. & Tuckerman, M. E. *Statistical Mechanics: Theory and Molecular Simulation*. Oxford Graduate Texts (Oxford University Press, Oxford, New York, 2023), second edition edn.

[29] Frenkel, D. & Smit, B. *Understanding Molecular Simulation: From Algorithms to Applications* (Elsevier, San Diego, 2002), second edition edn.

[30] Nosé, S. A unified formulation of the constant temperature molecular dynamics methods. *The Journal of Chemical Physics* **81**, 511–519 (1984).

[31] Hoover, W. G. Canonical dynamics: Equilibrium phase-space distributions. *Physical Review A* **31**, 1695–1697 (1985).

[32] Bussi, G., Donadio, D. & Parrinello, M. Canonical sampling through velocity rescaling. *The Journal of Chemical Physics* **126**, 014101 (2007).

[33] Laio, A. & Parrinello, M. Escaping free-energy minima. *Proceedings of the National Academy of Sciences* **99**, 12562–12566 (2002).

[34] Laio, A. & Gervasio, F. L. Metadynamics: A method to simulate rare events and reconstruct the free energy in biophysics, chemistry and material science. *Reports on Progress in Physics* **71**, 126601 (2008).

[35] Barducci, A., Bussi, G. & Parrinello, M. Well-Tempered Metadynamics: A Smoothly Converging and Tunable Free-Energy Method. *Physical Review Letters* **100**, 020603 (2008).

[36] How the Panama Canal Works. https://waitbutwhy.com/2014/09/panama-canal-works.html.

[37] Sholl, D. S. & Steckel, J. A. *Density Functional Theory: A Practical Introduction* (John Wiley & Sons, 2011).

[38] Koch, W. & Holthausen, M. C. *A Chemist's Guide to Density Functional Theory* (John Wiley & Sons, 2015).

[39] Bursch, M., Mewes, J.-M., Hansen, A. & Grimme, S. Best-Practice DFT Protocols for Basic Molecular Computational Chemistry. *Angewandte Chemie International Edition* **61**, e202205735 (2022).

[40] Perdew, J. P., Burke, K. & Ernzerhof, M. Generalized Gradient Approximation Made Simple. *Physical Review Letters* **77**, 3865–3868 (1996).

[41] Grimme, S., Bannwarth, C. & Shushkov, P. A Robust and Accurate Tight-Binding Quantum Chemical Method for Structures, Vibrational Frequencies, and Noncovalent Interactions of Large Molecular Systems Parametrized for All spd-Block Elements (Z = 1–86). *Journal of Chemical Theory and Computation* **13**, 1989–2009 (2017).

[42] Bannwarth, C. *et al.* Extended tight-binding quantum chemistry methods. *WIREs Computational Molecular Science* **11**, e1493 (2021).

[43] Bishop, C. M. & Bishop, H. *Deep Learning: Foundations and Concepts* (Springer Nature, 2023).

[44] Duval, A. *et al.* A Hitchhiker's Guide to Geometric GNNs for 3D Atomic Systems (2024). 2312.07511.

[45] Batatia, I. *et al.* The Design Space of E(3)-Equivariant Atom-Centered Interatomic Potentials (2022). 2205.06643.

[46] Batzner, S. *et al.* E(3)-equivariant graph neural networks for data-efficient and accurate interatomic potentials. *Nature Communications* **13**, 2453 (2022).

[47] Musaelian, A. *et al.* Learning local equivariant representations for large-scale atomistic dynamics. *Nature Communications* **14**, 579 (2023).

[48] Geiger, M. & Smidt, T. E3nn: Euclidean Neural Networks (2022). 2207.09453.

[49] Jo, S., Kim, T., Iyer, V. G. & Im, W. CHARMM-GUI: A web-based graphical user interface for CHARMM. *Journal of Computational Chemistry* **29**, 1859–1865 (2008).

[50] Kern, N. R., Lee, J., Choi, Y. K. & Im, W. CHARMM-GUI Multicomponent Assembler for modeling and simulation of complex multicomponent systems. *Nature Communications* **15**, 5459 (2024).

[51] Kim, S. *et al.* CHARMM-GUI ligand reader and modeler for CHARMM force field generation of small molecules: CHARMM-GUI Ligand Reader and Modeler for CHARMM Force Field Generation of Small Molecules. *Journal of Computational Chemistry* **38**, 1879–1886 (2017).

[52] Haynes, W. M. *CRC Handbook of Chemistry and Physics* (CRC Press, 2016).

[53] Bernetti, M. & Bussi, G. Pressure control using stochastic cell rescaling. *The Journal of Chemical Physics* **153**, 114107 (2020).

[54] Abraham, M. J. *et al.* GROMACS: High performance molecular simulations through multi-level parallelism from laptops to supercomputers. *SoftwareX* **1–2**, 19–25 (2015).

[55] Huang, J. *et al.* CHARMM36m: An improved force field for folded and intrinsically disordered proteins. *Nature Methods* **14**, 71–73 (2017).

[56] Kühne, T. D. *et al.* CP2K: An electronic structure and molecular dynamics software package - Quickstep: Efficient and accurate electronic structure calculations. *The Journal of Chemical Physics* **152**, 194103 (2020).

[57] Tribello, G. A., Bonomi, M., Branduardi, D., Camilloni, C. & Bussi, G. PLUMED 2: New feathers for an old bird. *Computer Physics Communications* **185**, 604–613 (2014).

[58] Grimme, S., Antony, J., Ehrlich, S. & Krieg, H. A consistent and accurate ab initio parametrization of density functional dispersion correction (DFT-D) for the 94 elements H-Pu. *The Journal of Chemical Physics* **132**, 154104 (2010).

[59] Grimme, S., Ehrlich, S. & Goerigk, L. Effect of the damping function in dispersion corrected density functional theory. *Journal of Computational Chemistry* **32**, 1456–1465 (2011).

[60] Goedecker, S., Teter, M. & Hutter, J. Separable dual-space Gaussian pseudopotentials. *Physical Review B* **54**, 1703–1710 (1996).

[61] Hartwigsen, C., Goedecker, S. & Hutter, J. Relativistic separable dual-space Gaussian pseudopotentials from H to Rn. *Physical Review B* **58**, 3641–3662 (1998).

[62] VandeVondele, J. *et al.* Quickstep: Fast and accurate density functional calculations using a mixed Gaussian and plane waves approach. *Computer Physics Communications* **167**, 103–128 (2005).

[63] CP2K_Developers. How to Converge the CUTOFF and REL_CUTOFF. https://manual.cp2k.org/trunk/methods/dft/cutoff.html.

[64] Makhmudov, A. Cp2k_to_extxyz: A script that helps in converting CP2K single-point calculations into an .extxyz file. https://github.com/almakhmudov/cp2k_to_extxyz.

[65] Thompson, A. P. *et al.* LAMMPS - a flexible simulation tool for particle-based materials modeling at the atomic, meso, and continuum scales. *Computer Physics Communications* **271**, 108171 (2022).

[66] Mir-group/pair_nequip. https://github.com/mir-group/pair_nequip.

[67] Morón, M. C., Prada-Gracia, D. & Falo, F. Macro and nano scale modelling of water–water interactions at ambient and low temperature: Relaxation and residence times. *Physical Chemistry Chemical Physics* **18**, 9377–9387 (2016).

[68] Marcos-Alcalde, I., Setoain, J., Mendieta-Moreno, J. I., Mendieta, J. & Gómez-Puertas, P. MEPSA: Minimum energy pathway analysis for energy landscapes. *Bioinformatics* **31**, 3853–3855 (2015).

[69] Granger, B. E. & Pérez, F. Jupyter: Thinking and Storytelling With Code and Data. *Computing in Science & Engineering* **23**, 7–14 (2021).

[70] Hunter, J. D. Matplotlib: A 2D Graphics Environment. *Computing in Science & Engineering* **9**, 90–95 (2007).

[71] Humphrey, W., Dalke, A. & Schulten, K. VMD: Visual molecular dynamics. *Journal of Molecular Graphics* **14**, 33–38 (1996).

[72] Jacobs, R. *et al.* A practical guide to machine learning interatomic potentials – Status and future. *Current Opinion in Solid State and Materials Science* **35**, 101214 (2025).

[73] Benayad, Z., David, R. & Stirnemann, G. Prebiotic chemical reactivity in solution with quantum accuracy and microsecond sampling using neural network potentials. *Proceedings of the National Academy of Sciences* **121**, e2322040121 (2024).

[74] Zeng, J. *et al.* DeePMD-kit v2: A software package for deep potential models. *The Journal of Chemical Physics* **159**, 054801 (2023).

Appendix A

Supplementary information

Table A.1: The plane-wave cutoff convergence test for DFT calculations. The calculation of ΔE involves subtracting the previous energy, e.g. $\Delta E(450\,\text{Ry}) = E(450\,\text{Ry}) - E(400\,\text{Ry})$. When the cutoff ≥ 800 and the rel cutoff ≥ 60, the error in total energy reduces to ca. 10^{-8} a.u. Only part of the results is shown for the sake of clarity.

Cutoff (Ry)	**Rel cutoff (Ry)**	**Total energy (a.u.)**	**ΔE (a.u.)**
400	60	-2352.6355962810	–
450	60	-2352.6262868887	9.31×10^{-3}
500	60	-2352.6262867349	1.54×10^{-7}
550	60	-2352.6254866602	8.00×10^{-4}
600	60	-2352.6243443853	1.14×10^{-3}
650	60	-2352.6242425582	1.02×10^{-4}
700	60	-2352.6224669798	1.78×10^{-3}
750	60	-2352.6209571227	1.51×10^{-3}
800	60	-2352.6212901605	-3.33×10^{-4}
850	60	-2352.6212901727	-1.22×10^{-8}
900	60	-2352.6212901873	-1.46×10^{-8}
950	60	-2352.6213082173	-1.80×10^{-5}
1000	60	-2352.6208957304	4.12×10^{-4}
10	800	-2354.4562984779	–
20	800	-2352.6775968461	1.78
30	800	-2352.6281701514	4.94×10^{-2}
40	800	-2352.6213637375	6.81×10^{-3}
50	800	-2352.6212892865	7.45×10^{-5}
60	800	-2352.6212901605	-8.74×10^{-7}
70	800	-2352.6212901729	-1.24×10^{-8}
80	800	-2352.6212901739	-1.00×10^{-9}
90	800	-2352.6212901739	0.00
100	800	-2352.6212901739	0.00

Algorithm A.1 Density-aware sampling of configurations

Input: Feature matrix $\mathbf{X} \in \mathbb{R}^{N\times 2}$ of N configurations, number of samples n_{samples}

1: Determine number of clusters:

$$k \leftarrow \max\left(10, \min\left(\left\lfloor \frac{N}{50} \right\rfloor, \left\lfloor \frac{n_{\text{samples}}}{10} \right\rfloor\right)\right)$$

2: Apply K-means clustering to $\mathbf{X}$ with k clusters
3: Initialize empty list for sampled cofiguration indices $S \leftarrow [\,]$
4: **for** each cluster C_i, $i = 1$ to k **do**
5: $\quad n_i \leftarrow \max\left(1, \left\lfloor \frac{|C_i|}{N} \cdot n_{\text{samples}} \right\rfloor\right)$
6: $\quad$ Select n_i random configurations from C_i with fixed random seed
7: $\quad$ Append selected indices to S
8: **end for**
9: **return** S

Output: List of selected configuration indices S

Table A.2: Composition of the full dataset used for training and testing. Well-tempered metadynamics settings used to run the simulations: [1]GFN1-xTB for energies and forces, gaussian height = 2 kcal/mol, spawning frequency = 25 fs^{-1}, bias factor = 30 and [2]NNP for energies and forces, gaussian height = 2 kcal/mol, spawning frequency = 50 fs^{-1}, bias factor = 30.

System	Temperature (K)	Simulation length (ps)	Train/Val	Test
MeDP[1]	300	50 ps	2000	150
MeDP[2]	300	100 ps	2000	150
MeDP[2]	320	500 ps	1000	300
MeDP[2]	340	500 ps	1000	300
MeHDP[1]	300	50 ps	2000	150
MeHDP[2]	300	100 ps	2000	150
MeHDP[2]	320	500 ps	1000	300
MeHDP[2]	340	500 ps	1000	300
Total			**12000**	**1800**

Quantum Chemistry and Physical Chemistry
Celestijnenlaan 200F bus 2404
3001 LEUVEN, BELGIË
tel. + 32 16 37 21 98
jeremy.harvey@kuleuven.be
www.kuleuven.be